The Viral Protein Corona Directs Viral Pathogenesis and Amyloid Aggregation

Kariem Ezzat[1,2], Maria Pernemalm[3], Sandra Pålsson[1], Thomas C. Roberts[4,5], Peter Järver[1], Aleksandra Dondalska[1], Burcu Bestas[2], Michal J. Sobkowiak[6], Bettina Levänen[7], Magnus Sköld[7,8], Elizabeth A. Thompson[9], Otto K. Kari[10], Tatu Lajunen[10], Yevheniia Ishchenko[11], Tarja Malm[11], Matthew J.A. Wood[4], Ultan F. Power[12], Sergej Masich[13], Anders Lindén[7], Johan K. Sandberg[6], Janne Lehtiö[3], Anna-Lena Spetz[1]*, Samir EL Andaloussi[2,4,14]*

[1]Department of Molecular Biosciences, The Wenner-Gren Institute, Stockholm University, Stockholm, Sweden.

[2]Department of Laboratory Medicine, Clinical Research Center, Karolinska Institutet, Stockholm, Sweden.

[3]Clinical Proteomics Mass Spectrometry, Department of Oncology-Pathology, Science for Life Laboratory, and Karolinska Institutet, Stockholm, Sweden

[4]Department of Physiology, Anatomy and Genetics, University of Oxford, Oxford, UK.

[5]Sanford Burnham Prebys Medical Discovery Institute, Development, Aging and Regeneration Program, La Jolla, CA, USA.

[6]Center for Infectious Medicine, Department of Medicine, Karolinska Institutet, Karolinska University Hospital Huddinge, Stockholm, Sweden.

[7]Institute of Environmental Medicine (IMM), Karolinska Institutet, Stockholm, Sweden.

[8] Department of Respiratory Medicine and Allergy, New Karolinska Solna, Karolinska University Hospital, Stockholm, Sweden.

[9] Department of Medicine, Immunology and Allergy Unit and Center for Molecular Medicine, Karolinska Institutet, Stockholm, Sweden.

[10]Drug Research Program, Division of Pharmaceutical Biosciences, Faculty of Pharmacy, University of Helsinki, Finland.

[11]A.I.Virtanen Institute for Molecular Sciences, University of Eastern Finland, Kuopio, Finland.

[12]Centre of Experimental Medicine, Queens' University Belfast, Belfast, United Kingdom.

[13]Department of Cell and Molecular Biology, Karolinska Institutet, Stockholm, Sweden.

[14]Evox Therapeutics Limited, Oxford Science Park, Oxford, UK.

*Equal contribution.

Correspondence should be addressed to KE: kariem.ezzat@su.se and A-LS: anna-lena.spetz@su.se

Abstract

Nanoparticles accumulate a layer of host factors on their surface (a protein corona) in biological fluids, which influences the nanoparticle activity. We hypothesized that viruses also constitute nanoparticles in this respect and here we provide evidence for the existence of viral protein coronae that have implications for viral infectivity, immune cell activation and catalysis of amyloid aggregation. We demonstrate that respiratory syncytial virus (RSV), a major cause of respiratory tract infections, accumulates a rich and distinctive protein corona in different biological fluids including human plasma, human bronchoalveolar lavage fluid, non-human primate plasma and fetal bovine serum. Additionally, corona pre-coating differentially affects viral infectivity and its ability to activate human monocyte-derived dendritic cells (moDCs) depending on the biological fluid. Furthermore, we demonstrate that RSV can bind and catalyze the amyloid aggregation of an amyloidogenic peptide derived from the islet amyloid polypeptide (IAPP) via surface-assisted (heterogeneous) nucleation. Similarly, we show that herpes simplex virus type 1 (HSV-1) possesses a protein corona and catalyzes the amyloid aggregation of the amyloid-beta ($A\beta_{42}$) peptide which is the major constituent of amyloid plaques in Alzheimer's disease (AD). We also show that HSV-1 infection increases $A\beta_{42}$ aggregation in the hippocampi and cortices of model AD animals. Our results provide a proof-of-concept for the presence of a viral protein corona layer that is dependent on the microenvironment and influences viral-host interactions. Additionally, the demonstration of corona-driven amyloid catalysis illustrates convergence between viral and amyloid pathologies in the extracellular environment suggesting a novel mechanistic link that warrants further investigation.

Keywords: protein corona, respiratory syncytial virus (RSV), herpes simplex virus type 1 (HSV-1), blood, epithelial lining fluid, Alzheimer's disease, amyloid

Introduction

The term "protein corona" refers to the layer of proteins that adhere to the surfaces of nanostructures when they encounter biological fluids. Nanoparticles adsorb biomolecules in biological fluids due to the high free energy of their surfaces [1]. The importance of the corona layer stems from the fact that it constitutes the actual surface of interaction with biological membranes or "what the cell sees" in the in-vivo context [2]. Hundreds of proteins have been identified to confer a distinct biological identity of nanoparticles in different microenvironments depending on their size, chemistry and surface modification (reviewed in [3–5]). These factors were found to be critical determinants of the biodistribution and pharmacodynamics of nanoparticles [6]. On the other hand, the ability of the surfaces of nanoparticles to partially denature certain corona proteins exposing "cryptic epitopes" highlights the role of the protein corona in the toxicology of nanoparticles [7–9]. The formation of a protein corona is particularly important in the context of nanoparticle interaction with amyloidogenic peptides such as amyloid beta ($A\beta_{42}$), α-synuclein and islet amyloid polypeptide (IAPP), which are associated with human diseases such as Alzheimer's disease (AD), Parkinson's disease and diabetes mellitus type 2 disease, respectively. Nanoparticles have been shown to catalyze amyloid formation via binding of amyloidogenic peptides in their corona, thereby increasing local peptide concentration and inducing conformational changes that facilitate fibril growth via a heterogenous nucleation mechanism [10–12]. This surface-assisted (heterogenous) nucleation has been demonstrated for several nanoparticles with different amyloidogenic peptides including IAPP, $A\beta_{42}$ and α-synuclein [11–14]. This catalytic process was also shown to be dependent on particle size, curvature and surface chemistry [15,16].

Here, we studied viruses in terms of their biophysical equivalence to synthetic nanoparticles in extracellular environments. As nanosized obligate intracellular pathogens, viruses lack any metabolic activity outside the cell, and can thus be expected to interact with host factors in the microenvironment similar to synthetic nanoparticles. In the current work, we used well-established techniques of nanotechnology to study the surface protein interactions of infectious viruses. We investigated the protein corona of respiratory syncytial virus (RSV) in comparison to herpes simplex virus type 1 (HSV-1) and synthetic liposomes. Additionally, we studied the interaction of both RSV and HSV-1 with amyloidogenic peptides.

RSV is an enveloped orthopneumovirus with a diameter between 100 and 300 nm and a single stranded negative-sense RNA genome with 10 genes encoding 11 proteins [17,18]. It is a leading cause of acute lower respiratory tract infections in young children worldwide, causing up to an annual estimate of 34 million cases [19]. By the first year of life, nearly 70% of children get infected with RSV at least once; and this percentage rises up to 90% by the second year of age causing up to 196,000 yearly fatalities [20]. Reinfection with RSV occurs throughout life, usually with mild local symptoms in the upper airways [21]. However, reinfection in the elderly and immunocompromised individuals can lead to severe clinical disease in the lower airways. While natural infection leads to the production of neutralizing antibodies, the ability of these antibodies to protect from subsequent RSV infections appears to be incomplete [22,23]. Neither a vaccine nor an antiviral therapy is yet available except for passive immunization using anti-RSV monoclonal antibodies such as palivizumab, which reduces RSV-associated hospitalization by 55% in infants at high risk [24,25]. Early vaccine trials using formalin-inactivated RSV led to enhanced disease with up to 80% of vaccinees being hospitalized and two dying [21,23]. This led to the hypothesis that the host immune responses play an important role in the pathophysiology of airway disease caused by RSV.

HSV-1 is an example of another virus with high prevalence, infecting nearly 70% of the human population [26]. HSV-1 is a double-stranded DNA virus consisting of an icosahedral nucleocapsid surrounded by tegument and envelope with virion sizes ranging from 155 to 240 nm [27]. HSV-1 is a neurotropic virus that infects peripheral sensory neurons and establishes latency [28]. Latent HSV-1 is occasionally reactivated causing peripheral pathology and under certain circumstances it can migrate into the central nervous system causing herpes simplex encephalitis; the most common cause of sporadic fatal viral encephalitis [28,29]. In the context of the current work we focused on the presumptive role of HSV-1 in the pathology of AD [30]. A number of risk factors have been associated with AD, including the E4 allele of the apolipoprotein E (Apo-E), diabetes, vascular pathology, neuroinflammation and infections [31]. Among the infections that have been implicated in AD, several recent studies have supported the theory of a significant role of HSV-1 in the disease [30]. HSV-1 DNA was found to be localized within AD amyloid plaques. In AD brains, 80% of the amyloid plaques contained HSV-1 DNA, while only 24% of the viral DNA was associated with plaques in normal aged brains [32]. In addition, the presence of anti-HSV IgM antibodies, which indicate HSV reactivation, is correlated with a high risk of AD [33]. Moreover, HSV-1 infection has been shown to promote neurotoxic Aβ accumulation in human neural cells and to the formation of Aβ deposits in the brains of infected mice [34]. Despite these correlations, to our knowledge, no evidence has been found supporting a direct role of HSV-1 in the process of amyloid aggregation.

In the present study, we demonstrated that upon encountering different biological fluids, RSV accumulated extensive and distinct protein coronae compared to HSV-1 and synthetic liposomes. The various coronae were dependent on the biological fluid and exerted markedly different effects on RSV infectivity and capacity to activate monocyte-derived dendritic cells **(**moDCs). Moreover, upon interaction with an amyloidogenic peptide derived from IAPP, RSV accelerated the process of amyloid aggregation via surface-assisted nucleation. This amyloid catalysis was also demonstrated for HSV-1 and the $A\beta_{42}$ peptide in-vitro and in an AD animal model. Our findings highlight the potential importance of viral protein corona interactions for viral pathogenesis and provide a direct mechanistic link between viral and amyloid pathologies.

Results

RSV accumulates distinctive protein coronae in different biological fluids

Based on the extensive literature describing the significant role of corona factors in synthetic nanoparticle functionality, we used established techniques to answer questions regarding RSV pathogenicity [35]. Using proteomics, we assessed the RSV protein corona profiles in human plasma (HP), human bronchoalveolar lavage fluid (BAL), rhesus macaque plasma (MP), and fetal bovine serum (FBS). These biological fluids represent different microenvironments encountered by the virus in terms of tissue tropism (HP vs. BAL), zoonosis (MP) and culturing conditions (FBS). Viral stocks were produced in serum-free conditions to prevent initial contamination with FBS proteins. Virions produced under serum-free conditions were incubated with 10% v/v solutions of different biological fluids. Controls included non-infected cell medium representing the background cellular secretome, and synthetic lipid vesicles of a size comparable to RSV (200 nm) with positively- and negatively charged surfaces. In addition, we compared the corona of RSV to HSV-1 to probe for differences between different viruses of relatively similar size. A schematic representation of the experimental design can be found in Supp. Fig.

1. After incubation for 1 h at 37 ˚C, the virions were re-harvested by centrifugation and washed twice before performing mass spectrometry-based proteomic analyses.

Assessment of the proteomic data by principle component analysis (PCA) showed that RSV and HSV-1 samples separated from another and that viral samples were well separated from the control samples with tight replicate (triplicate) grouping (Fig. 1 and Supp. Fig. 2). In order to determine if the most abundant corona factors were the most abundant proteins in the biological fluids, the crude fluids were also analyzed by mass spectrometry. The top 10 most abundant proteins identified are presented Table 1 and Supp. Table 1 for RSV and HSV-1, respectively. Similar to previous findings for nanoparticles [36], our data showed that the most abundant proteins in the protein corona were not necessarily the most abundant in the biological fluids. This, together with the PCA analyses comparing RSV to HSV-1 to the controls, indicates enrichment of particular corona factors depending on the surface properties of the virus. Moreover, proteomic data sets were visualized by heat map and hierarchical clustering revealing an extensive protein corona signature for viral samples in each biological fluid (Fig. 1D). While the serum-free viral particles contain some host factors that are incorporated during virus replication and budding from the cells, the virus was able to subsequently accumulate a different set of host factors which were dependent on the biological fluid. As such, a characteristic protein fingerprint was associated with each biological fluid. The viral corona factors present in each biological fluid are listed in Supp. Table 2.

Additionally, we used transmission-electron microscopy (TEM) to visualize the viral corona. A layer of factors was observed interacting with the viral surface upon encounter with cell membranes in HP and FBS conditions, which was absent in serum free conditions (Fig. 2). We also performed cryoimmunoelectron microscopy using antibodies for certain proteins that were detected in the viral corona proteomic analysis. In serum-free conditions, we used an anti-RSV F-protein antibody. For HP and BAL coronae, we used anti-human IgG and anti-surfactant protein A antibodies, respectively. The bound antibodies were detected using secondary antibodies coated with 10 nm gold nanoparticles. As shown in Supp. Fig. 3, corona factors were bound to the surface of RSV and labelled with the respective antibodies. Taken together, the electron microscopy studies demonstrated that RSV accumulated a layer of corona factors that are likely to be involved in cellular interactions.

The protein corona influences viral infectivity and moDC activation

To investigate if differential corona composition affects viral infectivity, virions produced under serum-free conditions were pre-incubated with different biological fluids before infection of HEp-2cells. The RSV-eGFP virions were incubated with biological fluids at a protein concentration of 0.3 mg/ml (equivalent to 5% v/v) for 1 h at 37 ˚C then diluted 10 times in serum-free medium before infecting the cells at final MOI of 1. Corona pre-coating had a significant effect on viral infectivity as demonstrated by the differential frequency of eGFP expressing cells quantified by flow cytometry (Fig. 3A-B and Supp. Fig 4). HP corona pre-coating significantly reduced infectivity compared to serum-free conditions, while FBS and MP led to 5-6 fold enhancement in infectivity. BAL corona also enhanced infectivity, but to a lower extent as compared to MP and FBS. Moreover, fluorescence microscopy revealed syncytia formation of cells infected with BAL, MP and FBS coronae (Supp. Fig. 5). No significant differences in cell-toxicity were observed. The effect of both FBS and MP corona on enhancement of RSV infectivity was concentration-dependent as shown in Supp. Fig. 6A. While the FBS corona enhancement increased with concentration, the MP effect decreased after a protein concentration of 0.3 mg/ml was

reached. This can be due to the increase of unbound corona factors that compete with bound factors for cellular receptors. Furthermore, we investigated the effect of corona pre-coating on viral neutralization via palivizumab, which is a humanized monoclonal antibody directed against the F protein of RSV. We found that the enhancing effects of the coronae were completely lost in the presence of the antibody and that the antibody neutralization curves were very simillar in the presence and the absence of the viral corona (Supp Fig. 6B). Importantly, this data demostrated that high affinity antibodies are able to compete out corona factors to impart host protection.

Furthermore, we investigated the effect of different coronae on the activation of human moDCs by quantifying the expression of the maturation marker CD86. Differentiated moDCs were infected by virions produced under serum-free conditions with different corona pre-coatings for 4h in serum-free conditions. The cells were then washed and incubated in serum-containing medium for 72 h prior to flow cytometry analyses. Only the BAL pre-coated virions were able to induce moDC activation and increase CD86 expression to levels similar to the TLR3 ligand polyI:C (Fig. 3C-F). Notably, adding BAL or RSV per se did not activate the cells, showing that it was the RSV-BAL corona complex that induced moDC activation. In addition, BAL pre-coating enhanced infectivity in moDCs as quantified by flow cytometry of eGFP expression (Fig. 3E-F). Altogether, this shows that pre-incubation of virions produced under serum-free conditions in different biological fluids to allow a corona formation greatly affects infectivity and the ability to induce moDC activation.

Differential RSV corona composition

As RS infects nearly 100% of the human population, it is expected that anti-RSV antibodies would be present in biological fluids of human origin. Indeed, both HP and BAL contained high levels of anti-RSV IgG antibodies as demonstrated by ELISA (Supp. Fig. 7). The set of factors that were only present in the HP corona and not in the other conditions comprised several antibodies and complement factors (highlighted in Fig. 4A). Moreover, gene list enrichment analyses of HP corona revealed an enrichment of immunological gene ontology (GO) terms such as complement activation and humoral immune response (Fig. 4B). The HP corona proteomic profile was consistent with the observed inhibition of infectivity (neutralization), indicating that the corona characterization methodology is representative of the actual layer of host factors that surrounds the viral particle.

Notably, despite having comparably high levels of virus-specific IgG antibodies, BAL imparted opposite effects on infectivity compared to HP. At the proteomics level, GO analysis revealed that the viral BAL corona comprised a different set of factors that are less enriched in immunological components and more enriched in factors related to adhesion, anchoring, protein targeting to membrane, interspecies interaction, mutualism through parasitism, protein complex binding, and macromolecular complex binding (Fig.4). On the other hand, both anti-RSV IgG negative FBS and MP enhanced viral infectivity several folds over serum-free conditions in HEp-2 cells. GO analysis revealed that FBS and MP coronae are also enriched in terms such as anchoring, adhesion, receptor binding, protein complex binding, unfolded protein binding, interspecies interaction, viral process, and mutualism through parasitism (Supp. Fig. 8).

RSV catalyzes amyloid aggregation

Since nanoparticles are known to bind amyloidogenic peptides in their coronae leading to induction of amyloid aggregation via a heterogenous nucleation mechanism, we next investigated whether viruses are also capable of

this particular corona interaction. We investigated the interaction of RSV with a model amyloidogenic peptide (NNFGAIL) derived from the IAPP. We traced the ability of RSV to accelerate amyloid kinetics using the well-established thioflavin T (ThT) based methodology. The ThT dye changes its fluorescence emission spectrum upon binding to amyloid fibrils, and plotting relative changes in the fluorescence intensity against time illustrates the kinetics of the amyloid formation process [37]. Using the ThT assay, we found that the presence of RSV particles significantly accelerated amyloid formation of NNFGAIL compared to non-infected cell supernatant demonstrating that RSV can act as a catalytic surface for amyloid aggregation (Fig. 5A). Additionally, extensive fiber networks were observed with TEM within 100 min. of incubation with RSV (Fig. 5B) and some virions were located at the tip of these fibers (Fig. 5C). Moreover, RSV catalytic activity was more efficient than lipid vesicles of similar size; however, it was dramatically reduced in the presence of 5% FBS, indicating a competition between the peptide and other corona factors for the viral surface (Fig. 5D). On the other hand, RSV failed to catalyze the amyloid aggregation of GNNQQNY peptide, which is derived from yeast prion protein (Fig. 5E). This, in turn, indicates that such interactions are not universal to all amyloidogenic peptides but display some selectivity depending on the virus/peptide pair.

HSV-1 accelerates the kinetics of $A\beta_{42}$ amyloid formation

The finding that viral surfaces can serve as catalysts for amyloid formation warranted further investigation and confirmation using another virus/peptide system. To this end, we investigated HSV-1 and the $A\beta_{42}$ peptide, whose aggregation is a major hallmark of AD. Recently, there has been an increasing body of reports suggestive of a correlation between HSV-1 infection and AD, reviewed in [30]. However, evidence of a direct role of HSV-1 in the process of amyloid nucleation and subsequent fibril growth is currently lacking.

We found that HSV-1 significantly accelerated amyloid formation of $A\beta_{42}$ compared to non-infected cell supernatant (Fig. 6A). The catalytic activity was reduced by the presence of FBS, also indicating a competition at the viral surface (Fig 6B). In addition, HSV-1 was more efficient than liposomes in accelerating the amyloid aggregation kinetics (Fig. 6C). Furthermore, the propensity of HSV-1 mediated amyloid catalysis is higher for the more amyloidogenic $A\beta_{42}$ peptide compared to the shorter, less amyloidogenic $A\beta_{40}$ peptide (Fig. 5D). As a control, we compared the kinetic curves of the virus-containing medium vs naked medium upon incubation with ThT alone without a peptide. As shown in Supp. Fig 9, the curves were very similar, indicating that the relative changes that we observe in the presence of amyloidogenic peptides are not due to unspecific interaction of the virions with the ThT dye. Moreover, amyloid induction was further confirmed by TEM demonstrating fibril formation within 100 mins of incubation with viral particles (Fig. 6E). Amyloid protofilaments and fibrils at different stages of elongation can be observed interacting with the viral surface. Fig. 6E1 and E2 show multiple fibrillary structures emerging from one viral particle. Some aggregates were located at the connection between the viral surface and the fibrils suggesting that a nucleation mechanism takes place on the surface, thereby sparking fibril elongation. Viral particles also interacted with fibrillar structures that are part of an extensive network of fibers as shown in Fig. 6E3 and E4. Importantly, to demonstrate the in-vivo relevance of our mechanistic findings, we intracranially infected transgenic 5XFAD mice with HSV-1. The 5XFAD mouse model is a widely-used AD model as it recapitulates many AD phenotypes with rapid onset of $A\beta_{42}$ aggregation that spreads to the hippocampus and cortex by six months of age [38]. We observed a significant increase in $A\beta_{42}$ accumulation in the hippocampi and cortices of HSV-1 infected mice 48h post infection (Fig. 6 F and G) in comparison with animals injected with non-

infected supernatant. Representative images of the amyloid staining demonstrate the dramatic difference in amyloid accumulation between infected and non-infected animals (Fig. 6H). These results validated our biophysical findings using the ThT assay and demonstrated that the viral corona-driven catalysis of amyloid aggregation can take place in in-vivo situations.

Discussion

Viruses rely on the cellular machinery of the host for replication, production of viral proteins, viral assembly and export out of the cell. However, outside cells, viruses share many biophysical properties with nanoparticles. Based on this biophysical equivalence, we hypothesized that viruses accumulate a rich and selective protein corona layer in the extracellular environment similar to nanoparticles. Examples of particular host factors that bind to viral surfaces have previously been described. For example, lipoproteins such as apolipoprotein E (Apo-E) were shown to be essential for hepatitis C virus (HCV) infection [39]. Furthermore, coagulation factors such as factor X were shown to directly bind adenovirus leading to liver tropism [40,41]. Other soluble components such as Gas6 were shown to contribute to the infectivity of lentiviral vectors even when pseudotyped with multiple types of envelope proteins [42]. Furthermore, soluble heparin sulfonated proteoglycans (HSPGs) were shown to enhance the infectivity of human papillomavirus (HPV) [43]. Interestingly, amyloids derived from prostatic acidic phosphatase (PAP) in semen were shown to enhance HIV-1 infectivity by several orders of magnitude [44]. These studies illustrate the significant role of host proteins that adhere to viral surfaces. However, to the best of our knowledge, there is no previous work that has comprehensively studied and characterized the entire corona of a virus in different biological fluids.

In this work, we used proteomics to study viral protein corona enrichment in different biological fluids. We investigated the RSV protein coronae in biological fluids that are relevant to viral tropism, zoonosis and culturing conditions. As RSV is a virus tropic to the respiratory tract, we compared the viral corona in human BAL versus HP from young healthy volunteers. We also investigated the RSV corona in plasma from rhesus macaques which are used as a model in RSV studies and vaccine development [45]. Moreover, we studied the corona in FBS, which is the most commonly used cell growth supplement for viral production and in-vitro studies. We compared the RSV corona to HSV-1 and lipid vesicles of similar size with positively or negatively charged surfaces as well as the biological fluids per se. PCA showed that the RSV corona profile was separated from that HSV-1 and lipid vesicles (Fig. 1). PCA analysis also showed good separation of HSV-1 and lipid vesicles (Supp. Fig. 2). Taken together and in accordance with previous corona nanoparticle literature[1], our analysis demonstrates the specific enrichment of differential corona profiles depending on the different surface properties, and that viruses are no exception to this phenomenon. In addition, while the viral corona profile was dependent on the biological fluid, it was not a mere reflection of the most abundant proteins as shown in the Table 1 and Supp. Table 1 of the top 10 proteins present in the viral coronae in comparison to crude biological fluids.

The viral protein corona was visualized using TEM, which revealed a layer surrounding the viral surface involved in cellular interactions (Fig. 2). Using cryoimmuno electron microscopy, we could detect specific protein hits from the proteomic analysis (human IgG in HP and surfactant protein A in BAL) on the surface of RSV upon incubation with HP or BAL, respectively (Supp. Fig. 3). Functionally, the coronae from the different biological fluids enhanced RSV infectivity except for the HP corona. In accordance with the biological activity, proteomic analysis

of the HP corona revealed that it was enriched in antibodies and complement factors (Fig. 1D & Fig. 4). In this regard, unbiased viral corona characterization might allow the detection of additional components of immunological importance for RSV neutralization. In contrast to the HP corona, the BAL corona enhanced viral infectivity in both HEp-2 cells and moDCs despite having equally high anti-RSV IgG antibody titers as compared to HP (Supp. Fig. 7). It can be speculated that the differential BAL corona profile might affect the formation of a neutralization complex, explaining pulmonary RSV reinfection even in individuals with high IgG titers [22]. An alternative, not mutually exclusive explanation is the presence of differential functional anti-RSV specific antibodies affecting RSV neutralization in BAL as compared to HP. We show here that the therapeutic anti-RSV antibody palivizumab was indeed capable of overcoming the viral corona layer. It remains to be elucidated, which avidity is required in order to compete out the corona layer.

Furthermore, pre-incubation of RSV with BAL was the only condition that induced moDC activation, while this was not observed for any of the controls using BAL per se, or other RSV conditions (Fig. 3). This demonstrates a role of corona factors in virus-induced immune activation that may contribute to disease pathophysiology. The list of proteins that are uniquely detected in the BAL corona included pulmonary surfactants which were shown to enhance RSV infectivity [46], nucleolin and EGFR, which were shown to be important for RSV cell entry [47,48], adhesion molecules (such as tetraspanin, neuroplastin, integrin and cadherin), coxsackievirus/adenovirus receptor, poliovirus receptor and zinc finger CCCH-type antiviral protein 1 (Fig. 4). Taken together, this shows that extracellular RSV can interact with microenvironmental factors forming a viral corona. As the corona layer is a rich and complex layer, the final biological effect is expected to be dependent on a multitude of corona factors rather than a single protein. Moreover, it is not the combination of the proteins in the biological fluids per se that affect the outcome but rather the protein layer building up around the virus, as shown by the lack of moDC activation by BAL fluid alone (Fig. 3).

Additional biological fluids investigated in our study included FBS and MP and they both enhanced the infectivity of RSV. GO analysis suggests a role of these corona factors in interspecies interaction, mutualism, viral process, protein complex binding, unfolded protein binding anchoring and adhesion. Factors in FBS that may contribute to these effects include C4b-binding protein alpha-like which is a complement inhibitor, isoform 2 of fermitin family homolog 2 which binds to membranes enriched in phosphoinositides and enhances integrin-mediated adhesion [49] and hepatitis A virus cellular receptor 1 (Supp. Fig. 8). In the MP corona, several adhesion proteins were found including: fibronectin isoform 4 preproprotein, endothelial cell-selective adhesion molecule, fermitin family homolog 3 short form and zyxin. The MP corona also includes receptor ligands such as: transferrin and C-X-C motif chemokine together with tetherin (isoform 2 of Bone marrow stromal antigen 2) which possesses antiviral properties based on its ability to tether viruses to the cell membrane preventing their release [50]. Taken together, this illustrates that the observed functional effects of the viral protein corona are most likely mediated by a combination of factors that are enriched on the viral surface and not by a single factor. Since many viruses bind to several receptors and co-receptors, such interactions might be taking place in a multivalent manner [51].

Notably, our results on FBS and MP show that viral pre-coating with a protein corona via straightforward exposure to low concentrations of biological fluids from different species can have a significant impact on infectivity. It highlights that viral protein corona has to be taken into consideration in relation to zoonotic studies and development of animal models as well as vaccine development processes that includes viral production.

We then investigated whether viral corona interactions with host factors involve surface-assisted nucleation of amyloidogenic peptides. Similar to other phase transition processes (such as crystallization for example), the process of amyloid formation is biphasic, with an initial rate-limiting nucleation phase followed by a rapid growth or elongation phase [37,52,53]. According to the classical nucleation theory, small molecular assemblies (nuclei) need to be formed within a supersaturated metastable phase (soluble peptide at high concentration) to enable the system to cross the energy barrier of transforming from one phase (liquid) to the another (amyloid fibers) [54,55]. Once formed, the nuclei push the system towards spontaneous self-assembly into the more stable and energetically favorable state of amyloid fibrils in reminiscence of the process of crystallization [53,55]. Nucleation can take place due to the spontaneous formation of nuclei within the bulk of a supersaturated phase, and in this case, it is termed homogeneous nucleation [54,56]. However, homogenous nucleation is a rare and slow process as it depends on the unlikely event of the spontaneous formation of a stable nucleus [52,55]. Practically, the more common mechanism of phase transition is via nucleation catalyzed by the presence of a foreign surface i.e. heterogenous nucleation [55,56]. In this regard, nanoparticles have been shown to act as catalytic surfaces that facilitate heterogenous nucleation of amyloid fibrils via binding, concentrating and enabling conformational changes of amyloidogenic peptides [10,15,55].

Similar to what have been reported with nanoparticles, we found that RSV accelerated the kinetics of amyloid aggregation of a model amyloidogenic peptide derived from IAPP (NNFGAIL). This demonstrates that viral particles are also capable of amyloid catalysis via surface-assisted heterogenous nucleation (Fig. 5). Notably, amyloidogenic peptides can also be found in the RSV corona profile in BAL and HP (isoform 2 of major prion protein) and in MP (amyloid beta A4 protein). This suggests that viral interaction with amyloidogenic peptides is feasible in complex biological fluids. In order to investigate if this catalytic mechanism extends to other virus-amyloid pairs, we evaluated whether HSV-1 could accelerate the amyloid kinetics of $A\beta_{42,}$ which is implicated in AD. Several recent studies have suggested HSV-1 involvement in AD [30]. Herein, we found that HSV-1 accelerated the kinetics of amyloid aggregation of $A\beta_{42}$ and to a lesser extent the aggregation of $A\beta_{40}$ (Fig. 6). HSV-1 was more efficient than lipid vesicles in amyloid catalysis and this efficiency decreased in the presence of FBS demonstrating a competition with other corona factors on the viral surface. Additionally, TEM demonstrated an interaction between amyloid fibrils at different stages of maturation and the viral surface via some aggregate intermediate, which we speculate represent the surface-assisted nucleation process. Importantly, infecting 5XFAD AD animal models with HSV-1 lead to increased accumulation of $A\beta_{42}$ plaques as evident by immunohistochemical analysis (Fig. 6), demonstrating that the viral corona-driven catalysis can take place in-vivo.

Taken together, our data on RSV and HSV-1 demonstrated that viruses can physically act as nano-surfaces capable of catalyzing amyloid nucleation and leading to accelerated fibril formation. While our results do not prove disease causality, they present mechanistic explanation of the clinical and experimental correlations drawn between HSV-1 and AD, which requires further investigation. Interestingly, Apo E, which is a well-known risk factor for AD, was enriched the HSV-1 corona, suggesting even further disease links (Supp. Table. 2).

Very recently, adding to the accumulating evidence of a role of herpes viruses in AD, a multiscale analysis study of different AD cohorts pointed to a disruption of molecular, genetic, and clinical networks by herpes viruses [57]. The authors interpret the correlation in the context of the "antimicrobial hypothesis" that suggests that Aβ is an antimicrobial peptide that is released to sequester infections [58]. This hypothesis has its roots in the "biflocculant hypothesis" suggested earlier, where Aβ is thought to be released to sequester neurotoxins in plaques [59]. Here, we

present an alternative but not mutually exclusive explanation. Our "corona-driven" hypothesis suggests that the virus interacts with extracellular amyloidogenic peptides as part of the pathogenesis, and the bound peptides do not necessarily possess an immunological and/or an antimicrobial function. This is further corroborated by studies showing that amyloids can enhance the infectivity for viruses such as HIV and HSV [44,60]. In this case, the virus will evolve to optimize these interactions via natural selection in order to maintain a chronic state of infectivity rather than avoiding them. In addition, the corona-driven viral surface-assisted nucleation mechanism could be extended to other viruses correlated with neurodegenerative pathology such as HIV and HIV-associated neurocognitive disorder (HAND)[61] and influenza virus and post-encephalitic parkinsonism [62]. Finally, the implication that viruses are capable of inducing conformational changes in bound host factors leading to exposure of cryptic epitopes may prove important for better understanding the correlation between viruses and autoimmune diseases.

To conclude, the current work was based on the biophysical equivalence between viruses and synthetic nanoparticles in extracellular environments. We here demonstrated that nanotechnological concepts such as the protein corona and surface-assisted nucleation can be extended to infectious viruses leading to novel insights on viral-host interactions. We showed that viral protein corona accumulation and amyloid catalysis are two aspects of the same phenomenon, namely viral surface interaction with extracellular host proteins. This phenomenon leads to the modulation of how viruses interact with cells and/or the induction of conformational changes in bound proteins that leads to accelerated amyloid aggregation. These findings highlight the potentially critical role of viral extracellular interactions in viral infectivity and in relation to extracellular protein pathology.

Materials and Methods

Viral and cell culture

HEp-2 cells, a human laryngeal carcinoma cell line, were used for RSV viral culture and infectivity experiments. Preparation of RSV A2-eGFP stocks was performed using VP-SFM serum-free, ultra-low protein medium containing no proteins, peptides, or other components of animal or human origin (ThermoFisher, USA). HEp-2 cells were initially seeded in growth medium (DMEM medium with 5% FBS (ThermoFisher, USA), 1% Penicillin/Streptomycin (ThermoFisher, USA) and 0.01M HEPES (SigmaAldrich, Germany) until they reached approximately 70-80% confluency. At the day of infection, the cells were washed twice with warm PBS and the medium was replaced with VP-SFM containing 50 μg/ml gentamycin. Cells were infected at MOI of 4 and incubated for 5-6 days until >90% eGFP expression was visible with fluorescence microscopy. Cells were then scraped, vortexed thoroughly, sonicated for 10 min., vortexed thoroughly one more time and spun at 1000 g for 5 min. The supernatant was transferred to new tubes and used freshly for the proteomics and amyloid interaction experiments. For long-term storage, infectivity and moDC activation experiments the supernatant was adjusted with $MgSO_4$ and HEPES (SigmaAldrich, Germany) solutions to a final concentration of 0.1M $MgSO_4$ and 50 mM HEPES. RSV was then concentrated using a 1.45 M sucrose cushions in the following buffer (1 M MgSO4; 50 mM Hepes, pH 7.5; 150 mM NaC1) according to [63] via centrifugation for 4 h at 7500 g at 4 ˚C. The viral concentrated layer was then harvested from interface between the cushion and the supernatant, aliquoted and immediately frozen at -80 ˚C. Quantifications of viruses were measured using real-time qPCR. Purification of viral RNA was performed using the QIAamp® Viral RNA extraction kit (QIAGEN) and extracted RNA was stored at

-80 ˚C. Viral titers were determined using the SuperScript® III Platinum® One-Step Quantitative real-time PCR system (Life Technologies) with the following probe and primers: RSV-A probe CAC CAT CCA ACG GAG CAC AGG AGA T (5'-labeled with 6-FAM and 3' labeled with BHQ1), RSV-A forward primer AGA TCA ACT TCT GTC ATC CAG CAA and RSV-A reverse TTC TGC ACA TCA TAA TTA GGA G. For initial viral quantification purposes, a commercially available RSV-A2 strain was purchased from (Advanced Biotechnologies Inc). The MOIs used for infectivity experiments were based on genome copies/ml measured by qPCR and the infectious viral titers were measured as $TCID_{50}$ on HEp-2 cells as described earlier [64]. Briefly, 10-fold dilutions of virus were added onto Hep2 cells for 2 h at 37°C, then inoculum was removed, and fresh maintenance medium was added. The plates were examined in the microscope on day7 and the number of wells for each dilution that was positive for GFP was noted. The titer was calculated according to the method of Karber. The viral stock of $7x10^8$ genome copies/ml corresponded to $\log_{10}$ 6.7 $TCID_{50}$/mL.

For HSV-1, strain F HSV-1 stocks were prepared by infecting African green monkey kidney (VERO) cells at 80–90% confluency in DMEM (Invitrogen) with 5% FBS or in serum-free DMEM. The virus was harvested 2 d after infection. Cells were subjected to two freeze-thaw cycles and spun at 20,000 g for 10 min to remove cell debris. Clarified supernatant was aliquoted and stored at -80°C until use. Non-infected cell medium was prepared with the same procedure without viral infection. Plaque assay was used to determine viral titers. 10-fold dilutions of virus were added onto VERO cells for 1 h at 37°C, then inoculum was removed, and fresh medium containing 0.5% carboxymethyl cellulose (Sigma Aldrich) was added. Cells were fixed and stained 2d later with a 0.1% crystal violet solution and the number of plaques was counted.

Human BAL samples

The use of human BAL samples for the current study was approved by the Regional Committee for Ethical Review in Stockholm (D. No 2016/1985-32). All donors had given oral and written informed consent to participate in the bronchoscopy study, in line with the Helsinki Declaration. The clinical characteristics of the utilized cohort of healthy volunteers were described in detail elsewhere [65]. Briefly, healthy subjects of male and female gender were recruited at the Lung Allergy Clinic, Karolinska University Hospital, Solna. These subjects were examined after denying regular tobacco smoking and history of allergy or lung disease during an interview. The final inclusion required that these subjects displayed no signs of pulmonary or disease during clinical examination, spirometry and clinical blood testing including electrolytes, white cell differential counts and C-reactive protein. Bronchoscopy with BAL (5 x 50 ml of sterile and phosphate-buffered saline) was performed according to clinical routine at Karolinska University Hospital, Solna, as previously described [65]. BAL was concentrated using 5 kDa cutoff 4 ml spin concentrator (Agilent Technologies, USA) before infectivity experiments.

Lipid vesicle preparation and characterization

1,2-distearoyl-sn-glycero-3-phosphocholine (DSPC), 1,2-dioleoyl-3-trimethylammonium-propane (DOTAP), 1,2-distearoyl-sn-glycero-3-phospho-(1'-rac-glycerol) (DSPG), and cholesterol were bought from Avanti Polar Lipids, Inc. (Alabaster, AL, USA). All other compounds were bought from Sigma-Aldrich (St. Louis, MO, USA). The lipids were dissolved in chloroform in molar ratios of 9:1 (DSPC / cholesterol) for neutral liposomes, 9:1 (DSPC / DOTAP) for cationic liposomes and 9:1 (DSPC / DSPG) for anionic liposomes. The liposomes were

formed by the thin film hydration method followed by extrusion through a polycarbonate membrane. Briefly, chloroform was evaporated by heating the sample tube to 65 °C and gradually reducing the pressure to 70 mbar under a nitrogen flow in a vacuum rotary evaporation system (Büchi R-114, Büchi Labortechnik AG, Flawil, Switzerland). The resulting thin lipid layer was hydrated with 500 µL of PBS by gently stirring the tube in a water bath (65 °C) for 1 h. The sample was then extruded 11 times (65 °C) through polycarbonate membrane (pore size of 200 nm) with a syringe extrusion device (Avanti Polar Lipids) after which the sample was quickly cooled down and stored in a refrigerator. The concentration of the samples was 19 µmol/mL. The size of the liposomes was analyzed with a Zetasizer APS dynamic light scattering automated plate sampler (Malvern Instruments, Malvern, United Kingdom). The concentration of liposomes was determined using Nanosight (Malvern, USA). The zeta potential was measured at 25 °C in DTS 1070 folded capillary cells with Zetasizer Nano ZS (Malvern Instruments).

Protein corona proteomics

FBS was obtained commercially (ThermoFisher, USA). HP was obtained and pooled from at least 3 different healthy donors. MP was obtained and pooled from at least three different Indian rhesus macaques that were RSV seronegative. Ethical permit Dnr N2 / 15, Institutionen för medicin, Karolinska University Hospital, Solna. All protein corona experiments described below were performed in technical triplicates. For the viral corona proteomic experiments, freshly-harvested serum-free RSV supernatant (not-sucrose cushion concentrated) containing 6.6 x 10^9 RSV genome equivalents or serum-free DMEM produced HSV-1 stocks (2.1 x 10^8 PFU/ml) was incubated with 10% v/v solutions of different biological fluids in for 1h at 37 ˚C. Before adding the viruses, all the biological fluid solutions were adjusted to 10 mM sodium citrate (SigmaAldrich, Germany) to prevent coagulation. As a control, uninfected cell supernatant prepared in a similar way was also incubated with the biological fluid solutions. For lipid vesicles, 3 x 10^{11} of 200 nm positively or negatively charged lipid vesicles were incubated with 10% solutions of biological fluids at similar conditions. After incubation, viral/nanoparticle corona complexes were spun at 20,000 g at 4 ˚C, supernatant removed, and the pellet resuspended in 1 ml PBS. The pellet was washed twice with PBS using the same centrifugation conditions then boiled at 95 ˚C for 5 min. before measuring the protein content using Micro BCA™ protein assay kit (ThermoFisher, USA). The viral/nanoparticle corona complexes were then resuspended in PBS and adjusted with ammonium bicarbonate to a final concentration of 20 mM. The samples were reduced by addition of 1:20 v/v 100 mM dithiothreitol (DTT) for 45 min. at 56 ˚C, and alkylated with 1:20 v/v 100 mM iodoacetamide (IAA) for 45 min at RT in the dark. Proteins were digested with trypsin (MS gold, Promega) 0,1 µg/µl overnight at 37 °C (trypsin : protein ratio 1:50). For sample clean-up, the samples were applied to strong cation exchange SCX microcolumns (Strata-XC Phenomenex). The microcolumns were initially washed with 100% methanol followed by MilliQ grade water. The samples were adjusted to >0.1% formic acid and then applied to the columns. After washing with 30% methanol and 0.1% formic acid the samples were eluted with 30% methanol and 5% ammonium hydroxide. Samples were dried in a SpeedVac and submitted to mass spectrometry (MS). For MS analysis, samples were dissolved in 3% ACN, 0.1% formic acid to end-concentration 1µg/µL. Two microliters of sample were analyzed with a hybrid LTQ-Orbitrap Velos mass spectrometer (ThermoFisher, USA). An Agilent HPLC 1200 system (Agilent) was used to provide the 70 min gradient. Data-dependent MS/MS (centroid mode) followed in two stages: first, the top-5 ions from the master scan were selected for collision induced dissociation with detection in the ion trap (ITMS); and then, the same 5 ions underwent higher energy collision dissociation (HCD) with detection in the Orbitrap (FTMS). The data was

searched by Sequest under the Proteome Discoverer 1.4.1.1.4 software (ThermoFisher) against the following Uniprot protein sequence databases; bos taurus version 170310, rhesus macaque version 170704, human version 160210, RSV version 160210 HHV1 version 180613, and Chlorocebus sabaeus version 180613 using a 1% peptide false discovery rate (FDR) cut-off limit. For samples containing proteins from multiple species, combined species databases were created by merging the corresponding protein databases. For label-free quantification, protein MS1 precursor area was calculated as the average of the top-three most intense peptides. Only proteins significantly detected (FDR 1%) in all three technical replicates in each sample were used in the downstream data analysis.

Data analysis

PCA analysis and hierarchical clustering of the filtered proteomics data (described above) was performed using ClustVis [66]. Gene ontology gene list enrichment analysis was performed using ToppFun [67]. For other experiments, non-parametric Kruskal-Wallis unpaired test was used followed by Dunn's post-test or Mann-Whitney test was used to compare the data. Six replicates from two independent experiments. P-value: ** $P \leq 0.01$. Statistics were calculated using GraphPad Prism 7 software.

ELISA

The detection of specific anti-RSV IgG antibodies in biological fluids was performed using Human Anti-Respiratory syncytial virus IgG ELISA Kit (ab108765, abcam®, Sweden), according to manufacturer's protocol. All biological fluids (FBS, HP, MP, BAL) were diluted to a protein concentration of 0.3 mg/ml before performing the assay and results were compared to the positive, cutoff, and negative controls provided by the kit manufacturer.

RSV infectivity

HEp-2 cells were seeded in maintenance medium until they reached 50-60% confluency. On the day of infection, the cells were washed twice with warm PBS and medium was changed to VP-SFM with gentamycin. Before adding to the cells, sucrose cushion-concentrated RSV stocks were pre-incubated with different biological fluids (FBS, HP, MP, BAL) at a final protein concentration of 0.3 mg/ml in VP-SFM with 10 mM sodium citrate for 1 h at 37 ˚C. The corona-precoated viruses were then added to the cells in serum-free conditions (diluted 10x) at a MOI of 1. 24 h post-infection, the medium was changed back to growth medium and cells were visualized with fluorescence microscopy 72 h post-infection. After visualization, the cells were washed and stained with LIVE/DEAD™ Fixable Far Red Dead Cell Stain Kit (ThermoFisher, USA) for 30 min at 4 ˚C in Dulbecco's phosphate-buffered saline (DPBS no calcium, no magnesium, ThermoFisher), then fixed and washed for flow cytometry using Cytofix/Cytoperm™ (BD, USA) according to manufacturer's protocol. Cells were then scraped and resuspended in DPBS, and the data was acquired using MACSQuant® Analyser 10 flowcytometer (Miltenyi Biotec, Sweden). The data was analyzed by FlowJo software (TreeStar) by excluding the dead cells stained with far-red fluorescent dye and subsequent calculation of GFP positive cells within the viable cell population. For experiments with palivizumab, cells were treated with different concentrations of the antibody before infection.

MoDC differentiation

Human monocytes were negatively selected from buffy coats using the RosetteSep Monocyte Enrichment Kit (1mL/10mL buffy coat; StemCell Technologies) and differentiated into moDC, using GM-CSF (250ng/mL;

PeproTech) and IL-4 (6.5ng/mL; R&D Systems) for 6 days in 37°C, 5% CO_2 at a density of $5x10^5$ cells/mL in RPMI 1640 completed with 10% FCS, 1mM sodium pyruvate, 10mM HEPES, 2mM L-glutamine, and 1% and penicillin/streptomycin (ThermoFisher, USA) as previously described [68]. Immature moDC were exposed to RSV pre-incubated with different biological fluids for 4h in serum free media, washed and then incubated in serum containing medium for 72 h before analyses of CD86 and RSV-eGFP expression. Dead cells were excluded using Live/Dead fixable near-IR dead cell stain kit (ThermoFisher). Flow cytometry sample data were acquired on a Fortessa (BD Biosciences) and the analysis was performed in FlowJo software (TreeStar).

Thioflavin-T Assay

NNFGAIL, GNNQQNY, $A\beta_{42}$, $A\beta_{40}$ were synthesized and purified by Pepscan (The Netherlands) and the final molecular weight was verified by MS. 10 µl of dimethyl sulfoxide (DMSO) (ThermoFisher, USA) were added to 1 mg aliquots of the peptide and running stocks were prepared in MQ water. ThT (Sigma Aldrich) was prepared at 4 mM in MQ water. For the assay, 150 µl/well ThT were added to black clear-bottom 96-well plates (Corning, USA), then 100 µl of freshly-harvested serum-free RSV supernatant (not-sucrose cushion concentrated) or serum-free DMEM produced HSV-1, controls, and lipid vesicles were added together with 50 µl of the different peptides. ThT fluorescence was measured at 440 nm excitation and 480 nm emission at 10-15 min. intervals (from bottom with periodic shaking) over 12-24 h on SpectraMax i3 microplate reader (Molecular Devices, USA). Curves were fitted using GraphPad Prism software.

Electron Microscopy

For cell sections with RSV, HEp-2 cells were seeded in 6 cm dishes in maintenance medium until 70-80% confluent, then washed and medium replaced with VP-SFM with gentamycin before infecting with RSV at MOI 100 in serum-free conditions or in 50% v/v of different biological fluids. Cells were then fixed with 2.5 % glutaraldehyde in 0.1M phosphate buffer, pH 7.4 at room temperature for 30 min. The cells were scraped off and transferred to an Eppendorf tube and further fixed overnight in the refrigerator. After fixation, cells were rinsed in 0.1M phosphate buffer and centrifuged (100g for 5 min.). The pellets were then fixed with 2% osmium tetroxide (TAAB, Berks, England) in 0.1M phosphate buffer, pH 7.4 at 4 ˚C for 2 h, then dehydrated in ethanol followed by acetone and embedded in LX-112 (Ladd, Burlington, Vermont, USA). Ultrathin sections (approximately 50-60 nm) were cut by a Leica EM UC 6 (Leica, Wien, Austria). Sections were stained with uranyl acetate followed by lead citrate and imaged in a Tecnai 12 Spirit Bio TWIN transmission electron microscope (FEI Company, Eindhoven, The Netherlands) at 100 kV. Digital images were captured by a Veleta camera (Olympus Soft Imaging Solutions, GmbH, Münster, Germany). For cryoimmunoelectron microscopy (iEM), cells were fixed in 3 % paraformaldehyde in 0.1 M phosphate buffer. Samples were then rinsed with 0.1M phosphate buffer and infiltrated in 10% gelatin. Then the specimens were infiltrated into 2.3 M sucrose and frozen in liquid nitrogen. Sectioning was performed at -95˚C and mounted on carbon-reinforced formvar-coated, 50 mesh Nickel grids. Immunolabelling was performed as follows: grids were placed directly on drops of 2% normal goat serum (DAKO, Glostrup, Denmark) in 0.1 M phosphate buffer to block non-specific binding then incubated with the primary antibodies: mouse anti-RSV fusion protein monoclonal antibody (Millipore, USA) or goat anti-human IgG (Licor, USA) or mouse anti-surfactant protein A antibody (abcam, ab51891). Antibodies were diluted 1:50 in 0.1M of phosphate buffer containing 0.1% normal goat serum overnight in a humidified chamber at room temperature. The

sections were washed using the same buffer and bound antibodies were detected using secondary antibodies coated with 10 nm gold (BBI solution, Analytic standard, Sweden) at a final dilution of 1:100. Sections were then rinsed in buffer and fixed in 2% glutaraldehyde, stained with 0,05% uranyl acetate, embedded in 1% methylcellulose and then examined in a Tecnai G2 Bio TWIN (FEI company, Eindhoven, The Netherlands) at 100 kV. Digital images were captured by a Veleta camera (Soft Imaging System GmbH, Műnster, Germany). For TEM of viruses with amyloids, 100 µl of RSV (3 x 10^8 genome copies/ml) or HSV-1 (2 x 10^7 PFU/ml) were incubated with 50µl 1mM NNFGAIL (for RSV) or 50µM $A\beta_{42}$ (for HSV-1) for 100 min. at 37 ˚C. Samples were applied to Formvar/carbon coated 200 mesh nickel grids (Agar Scientific, UK), then negatively stained using an aqueous solution of uranyl acetate (1%) and visualized.

Animal experiments

To evaluate the impact of the HSV-1 on brain β-amyloid (Aβ) levels, 3-month-old transgenic 5XFAD mice (purchased from Jackson Laboratories, Bar Harbor, Maine, US) were randomly divided into 2 groups. The animals were injected either with the HSV virus or non-infected supernatant using a micro-infusion pump (The Harvard Apparatus Pump Series, Harvard Bioscience, USA) into the right lateral ventricles as previously described [69]. Briefly, surgical anaesthesia was induced with 5% isoflurane and maintained with 1.8% isoflurane (in 30% O_2/70% N_2O). The temperature of the animals was maintained at 37 +/- 0.5 °C using a thermostatically controlled heating blanket connected to a rectal probe (PanLab, Harvard Apparatus, Barcelona, Spain). The skin was opened and the scull exposed. A small hole approximately 1 mm in diameter was drilled into the following coordinates: m/l (medial/lateral) +1.1 mm, a/p (anterior/posterior) −0.3 mm, d/v (dorsal/ventral) −2.0 mm. The mice were infused with either 10 µl of HSV-1 virus (2 x 10^7 PFU/ml) or with non-infected supernatant as control. After injection the wound was sutured and the animals placed in individual cages to recover for 48h. All animal work was approved by the Animal Care and Use Committee of the University of Eastern Finland (Kuopio) and performed according to the guidelines of National Institutes of Health for animal care. Mice were euthanized at 48 h after ICV (intracerebroventricular) infusion for tissue collection. The mice were anesthetized with an overdose of Avertin followed by transcardial perfusion with heparinized saline (2500 IU/L). The ICV infused brain hemisphere were removed and post-fixed in 4% PFA followed by cryoprotection in 30% sucrose. The hemibrains were frozen in liquid nitrogen and cryosectioned into 20-µm sagittal sections and stored in the anti-freeze solution. Six consecutive sagittal brain sections at 400 µm intervals were selected for immunohistological staining from each mouse. Aβ deposits were detected using primary anti-body specific to isoforms Aβ 37-42 (Aβ D54D2 XP, Cell Signaling Technology, 1:100 dilution, overnight at RT) and further visualized by fluorescent Alexa 568 secondary antibody (1:500 dilution, ThermoFisher Scientific). For quantification of Aβ immunoreactivities, the stained sections were imaged using 10x magnification in Zeiss Axio ImagerM.2 microscope equipped with Axiocam 506 mono CCD camera (Carl Zeiss, Oberkochen, Germany) running ZEN software (Carl Zeiss) for tailing and stitching of the images. Cortical and hippocampal Aβ immunoreactivities were quantified from 6 stained sections at 400 um intervals per animal using MatLab (MathWorks, MatLab 2017b). The accuracy of the analysis was confirmed by re-analyzing the images using ImageJ 1.50i software.

References

1. Monopoli, M. P., Aberg, C., Salvati, A. & Dawson, K. a. Biomolecular coronae provide the biological identity of nanosized materials. *Nat. Nanotechnol.* **7,** 779–86 (2012).

2. Walczyk, D., Bombelli, F. B., Monopoli, M. P., Lynch, I. & Dawson, K. A. What the cell 'sees' in bionanoscience. *J. Am. Chem. Soc.* **132,** 5761–5768 (2010).

3. Lee, B. J., Nguyen, V. H. & Lee, B. J. Protein corona : a new approach for nanomedicine design. *Int. J. Nanomedicine* **12,** 3137–3151 (2017).

4. Neagu, M. *et al.* Protein bio-corona: critical issue in immune nanotoxicology. *Arch. Toxicol.* **91,** 1–18 (2016).

5. Ke, P. C., Lin, S., Parak, W. J., Davis, T. P. & Caruso, F. A Decade of the Protein Corona. *ACS Nano* **11,** 11773–11776 (2017).

6. Caracciolo, G., Farokhzad, O. C. & Mahmoudi, M. Biological Identity of Nanoparticles In Vivo: Clinical Implications of the Protein Corona. *Trends in Biotechnology* **35,** 257–264 (2017).

7. Mortimer, G. M. *et al.* Cryptic epitopes of albumin determine mononuclear phagocyte system clearance of nanomaterials. *ACS Nano* **8,** 3357–66 (2014).

8. Lynch, I., Dawson, K. A. & Linse, S. Detecting Cryptic Epitopes Created by Nanoparticles. *Sci. STKE* (2006). doi:10.1126/stke.3272006pe14

9. Lira, A. *et al.* Binding kinetics of ultrasmall gold nanoparticles with proteins. *Nanoscale* (2018). doi:10.1039/C7NR06810G

10. Linse, S. *et al.* Nucleation of protein fibrillation by nanoparticles. *Proc. Natl. Acad. Sci. U. S. A.* **104,** 8691–8696 (2007).

11. Cabaleiro-Lago, C., Quinlan-Pluck, F., Lynch, I., Dawson, K. A. & Linse, S. Dual effect of amino modified polystyrene nanoparticles on amyloid beta protein fibrillation. *ACS Chem. Neurosci.* **1,** 279–287 (2010).

12. Gladytz, A., Abel, B. & Risselada, H. J. Gold-Induced Fibril Growth: The Mechanism of Surface-Facilitated Amyloid Aggregation. *Angew. Chemie Int. Ed.* 1–6 (2016). doi:10.1002/anie.201605151

13. Álvarez, Y. D. *et al.* Influence of gold nanoparticles on the kinetics of α-synuclein aggregation. *Nano Lett.* **13,** 6156–6163 (2013).

14. Habchi, J. *et al.* Cholesterol catalyses Aβ42 aggregation through a heterogeneous nucleation pathway in the presence of lipid membranes. *Nat. Chem.* (2018). doi:10.1038/s41557-018-0031-x

15. Mahmoudi, M., Kalhor, H. R., Laurent, S. & Lynch, I. Protein fibrillation and nanoparticle interactions: opportunities and challenges. *Nanoscale* **5,** 2570–88 (2013).

16. Terakawa, M. S., Yagi, H., Adachi, M., Lee, Y. H. & Goto, Y. Small liposomes accelerate the fibrillation of amyloid beta (1- 40). *J. Biol. Chem.* **290,** 815–826 (2015).

17. Bächi, T. & Howe, C. Morphogenesis and ultrastructure of respiratory syncytial virus. *J. Virol.* **12,** 1173–80 (1973).

18. Radhakrishnan, A. *et al.* Protein analysis of purified respiratory syncytial virus particles reveals an important role for heat shock protein 90 in virus particle assembly. *Mol. Cell. Proteomics* **9,** 1829–1848 (2010).

19. Nair, H. *et al.* Global burden of acute lower respiratory infections due to respiratory syncytial virus in young children: a systematic review and meta-analysis. *Lancet* **375,** 1545–1555 (2010).

20. McDermott, D. S., Weiss, K. A., Knudson, C. J. & Varga, S. M. Central role of dendritic cells in shaping the adaptive immune response during respiratory syncytial virus infection. *Futur. Virol* **6,** 963–973 (2011).

21. Collins, P. L. & Graham, B. S. Viral and Host Factors in Human Respiratory Syncytial Virus Pathogenesis. *J. Virol.* **82,** 2040–2055 (2008).

22. Hall, C. B., Walsh, E. E., Long, C. E. & Schnabel, K. C. Immunity to and frequency of reinfection with respiratory syncytial virus. *J. Infect. Dis.* **163,** 693–698 (1991).

23. Graham, B. S. Biological Challenges and Technological Opportunities for RSV Vaccine Development. *Immunol. Rev.* **239,** 149–166 (2011).

24. Cardenas, S., Auais, A. & Piedimonte, G. Palivizumab in the prophylaxis of respiratory syncytial virus infection. *Expert Rev. Anti. Infect. Ther.* **3,** 719–26 (2005).

25. Kim, L. *et al.* Identifying gaps in respiratory syncytial virus disease epidemiology in the United States Prior to the introduction of vaccines. *Clin. Infect. Dis.* **65,** 1020–1025 (2017).

26. Roizman, B. *Human Herpesviruses: Biology, Therapy and Immunoprophylaxis*. *Human Herpesviruses: Biology, Therapy, and Immunoprophylaxis* (2007). doi:10.2277/0521827140

27. Laine, R. F. *et al.* Structural analysis of herpes simplex virus by optical super-resolution imaging. *Nat. Commun.* **6,** 5980 (2015).

28. Menendez, C. M. & Carr, D. J. J. Defining nervous system susceptibility during acute and latent herpes simplex virus-1 infection. *J. Neuroimmunol.* **308,** 43–49 (2017).

29. Zuo, X., Tang, W., Chen, X. & Huang, W. A review with comments on herpes simplex encephalitis in adults. 24–27 (2017). doi:10.20517/2347-8659.2016.34

30. Piacentini, R. *et al.* HSV-1 and Alzheimer's disease: More than a hypothesis. *Front. Pharmacol.* **5,** 1–9 (2014).

31. Santos, C. Y. *et al.* Pathophysiologic relationship between Alzheimer's disease, cerebrovascular disease, and cardiovascular risk: A review and synthesis. *Alzheimer's Dement. Diagnosis, Assess. Dis. Monit.* **7,** 69–87 (2017).

32. Wozniak, M. A. & Itzhaki, R. F. Herpes simplex virus type 1 DNA is located within Alzheimer's disease amyloid plaques. *J. Pathol.* **220,** 114–125 (2010).

33. Lövheim, H., Gilthorpe, J., Adolfsson, R., Nilsson, L.-G. & Elgh, F. Reactivated herpes simplex infection increases the risk of Alzheimer's disease. *Alzheimers. Dement.* **11,** 1–7 (2014).

34. Wozniak, M. A., Itzhaki, R. F., Shipley, S. J. & Dobson, C. B. Herpes simplex virus infection causes cellular beta amyloid accumulation and secretase upregulation. *Neurosci. Lett.* **429,** 95–100 (2007).

35. Tenzer, S. *et al.* Rapid formation of plasma protein corona critically affects nanoparticle pathophysiology. *Nat. Nanotechnol.* **8,** 772–81 (2013).

36. Whitwell, H. *et al.* Nanoparticles in the Lung and their Protein Coron: The Few Proteins that Count. *Nanotoxicology* **5390,** (2016).

37. Arosio, P., Knowles, T. P. J. & Linse, S. On the lag phase in amyloid fibril formation. *Phys. Chem. Chem. Phys.* **17,** 7606–7618 (2015).

38. Oakley, H. *et al.* Intraneuronal beta-Amyloid Aggregates, Neurodegeneration, and Neuron Loss in Transgenic Mice with Five Familial Alzheimer's Disease Mutations: Potential Factors in Amyloid Plaque Formation. *J. Neurosci.* **26,** 10129–10140 (2006).

39. Chang, K.-S., Jiang, J., Cai, Z. & Luo, G. Human apolipoprotein e is required for infectivity and production of hepatitis C virus in cell culture. *J. Virol.* **81,** 13783–13793 (2007).

40. Waddington, S. N. *et al.* Adenovirus serotype 5 hexon mediates liver gene transfer. *Cell* **132,** 397–409 (2008).

41. Doronin, K. *et al.* Coagulation factor X activates innate immunity to human species C adenovirus. *Science* **338,** 795–8 (2012).

42. Morizono, K. *et al.* The soluble serum protein Gas6 bridges virion envelope phosphatidylserine to the TAM receptor tyrosine kinase Axl to mediate viral entry. *Cell Host Microbe* **9,** 286–98 (2011).

43. Surviladze, Z., Dziduszko, A. & Ozbun, M. A. Essential roles for soluble virion-associated heparan sulfonated proteoglycans and growth factors in human papillomavirus infections. *PLoS Pathog.* **8,** (2012).

44. Münch, J. *et al.* Semen-Derived Amyloid Fibrils Drastically Enhance HIV Infection. *Cell* **131,** 1059–1071 (2007).

45. Taylor, G. Animal models of respiratory syncytial virus infection. *Vaccine* **35,** 469–480 (2017).

46. Hickling, T. P. *et al.* Lung surfactant protein A provides a route of entry for respiratory syncytial virus into host cells. *Viral Immunol* **13,** 125–135 (2000).

47. Tayyari, F. *et al.* Identification of nucleolin as a cellular receptor for human respiratory syncytial virus. *Nat. Med.* **17,** 1132–1135 (2011).

48. Currier, M. G. *et al.* EGFR Interacts with the Fusion Protein of Respiratory Syncytial Virus Strain 2-20 and Mediates Infection and Mucin Expression. *PLoS Pathog.* **12,** 1–22 (2016).

49. Qu, H. *et al.* Kindlin-2 regulates podocyte adhesion and fibronectin matrix deposition through interactions with phosphoinositides and integrins. *J. Cell Sci.* **124,** 879–891 (2011).

50. Kuhl, B. D., Cheng, V., Wainberg, M. A. & Liang, C. Tetherin and its viral antagonists. *Journal of Neuroimmune Pharmacology* **6,** 188–201 (2011).

51. Wickham, T. J., Granados, R. R., Wood, H. a, Hammer, D. a & Shuler, M. L. General analysis of receptor-mediated viral attachment to cell surfaces. *Biophys. J.* **58,** 1501–1516 (1990).

52. Eisenberg, D. & Jucker, M. The amyloid state of proteins in human diseases. *Cell* **148,** 1188–1203 (2012).

53. Mezzenga, R. & Adamcik, J. The Amyloid Polymorphism in the Protein Folding and Aggregation Energy Landscape. *Angew. Chemie* (2018). doi:10.1002/ange.201713416

54. Vekilov, P. G. Nucleation. *Cryst. Growth Des.* **10,** 5007–5019 (2010).

55. Buell, A. K. *The Nucleation of Protein Aggregates - From Crystals to Amyloid Fibrils*. *International Review of Cell and Molecular Biology* **329,** (Elsevier Inc., 2017).

56. Kamano, Y., Kadota, K., Shimosaka, A., Shirakawa, Y. & Hidaka, J. Quantitative evaluation on the heterogeneous nucleation of amino acid by a thermodynamic analysis. *J. Mol. Liq.* **200,** 474–479 (2014).

57. Readhead, B. *et al.* Multiscale Analysis of Independent Alzheimer's Cohorts Finds Disruption of Molecular, Genetic, and Clinical Networks by Human Herpesvirus. *Neuron* 1–19 (2018). doi:10.1016/j.neuron.2018.05.023

58. Kumar, D. K. V. *et al.* Amyloid-beta peptide protects against microbial infection in mouse and worm models of Alzheimers disease. *Sci. Transl. Med.* **8,** 34072–34072 (2016).

59. Robinson, S. R. & Bishop, G. M. Aβ as a bioflocculant: Implications for the amyloid hypothesis of Alzheimer's disease. *Neurobiol. Aging* **23,** 1051–1072 (2002).

60. Wojtowicz, W. M. *et al.* Stimulation of enveloped virus infection by β-amyloid fibrils. *J. Biol. Chem.* **277,** 35019–35024 (2002).

61. Clifford, D. B. & Ances, B. M. HIV-associated neurocognitive disorder. *Lancet. Infect. Dis.* **13,** 976–86 (2013).

62. Jang, H., Boltz, D. A., Webster, R. G. & Smeyne, R. J. Viral parkinsonism. *Biochimica et Biophysica Acta - Molecular Basis of Disease* **1792,** 714–721 (2009).

63. Mbiguino, a & Menezes, J. Purification of human respiratory syncytial virus: superiority of sucrose gradient over percoll, renografin, and metrizamide gradients. *J. Virol. Methods* **31,** 161–70 (1991).

64. Broadbent, L. *et al.* In vitro modeling of RSV infection and cytopathogenesis in well-differentiated human primary airway epithelial cells (WD-PAECs). in *Methods in Molecular Biology* **1442,** 119–139 (Humana Press, New York, NY, 2016).

65. Che, K. F. *et al.* Interleukin-26 in antibacterial host defense of human lungs effects on neutrophil mobilization. *Am. J. Respir. Crit. Care Med.* **190,** 1022–1031 (2014).

66. Metsalu, T. & Vilo, J. ClustVis: a web tool for visualizing clustering of multivariate data using Principal Component Analysis and heatmap. *Nucleic Acids Res.* **43,** W566–W570 (2015).

67. Chen, J., Bardes, E. E., Aronow, B. J. & Jegga, A. G. ToppGene Suite for gene list enrichment analysis and candidate gene prioritization. *Nucleic Acids Res.* **37,** W305–W311 (2009).

68. Sköld, A. E. *et al.* Single-stranded DNA oligonucleotides inhibit TLR3-mediated responses in human monocyte-derived dendritic cells and in vivo in cynomolgus macaques. *Blood* **120,** 768–77 (2012).

69. DeVos, S. L. & Miller, T. M. Direct intraventricular delivery of drugs to the rodent central nervous system. *J. Vis. Exp.* e50326 (2013). doi:10.3791/50326

Acknowledgements

We would like to acknowledge the Svenska Sällskapet för Medicinsk Forskning (SSMF) for supporting Kariem Ezzat, Swedish Research Council (K2015-99X-22880-01-6) and Stockholm University for supporting Anna-Lena Spetz, Vetenskapsrådet, SSMF, and the Swedish foundation for Strategic Research for supporting Samir EL-Andaloussi, Dr. Michael N. Teng at the University of South Florida for providing the RSV-GFP virus, Professor Arto Urtti at the University of Helsinki for the lipid vesicles, the Instumentarium Science Foundation for supporting Otto K. Kari, the service of the Electron Tomography Facility at Karolinska Institutet, and the Academy of Finland for supporting the research of Tarja Malm. Anders Lindén obtained project funding from the Swedish Heart-Lung Foundation (No. 20150303), the Swedish Research Council (No. 2016-01653), as well as federal funding from Karolinska Institutet and through the Regional Agreement on Medical Training and Clinical Research (ALF, No. 20140309) between Stockholm County Council and Karolinska Institutet. No funding was obtained from the tobacco industry.

Figure Legends

Figure 1. Viral corona proteomics (A-C) Principal component analyses (PCA) of the corona proteomic profiles of RSV, HSV-1 and controls. Triplicate samples were incubated with 10% solutions of each different biological fluid for 1h at 37 ˚C, then re-harvested, washed and finally analyzed by MS. NI= Non-Infected supernatant, (-)Lipo = negatively charged lipid vesicles, 200 nm, (+)Lipo = positively charged lipid vesicles, 200 nm. (**A**) PCA comparing proteomic profiles in human plasma (HP) (**B**) PCA comparing proteomic profiles in fetal bovine serum (FBS) (**C**) PCA comparing the corona profiles of RSV in different biological fluids; HP, FBS, MP or BAL. (**D**) Heat map representing the viral corona fingerprints of RSV after incubation in different biological fluids. The three columns in the heatmap show three replicates. Red and blue indicate higher and lower than the mean protein signal, respectively. Scale bars represent row Z-scores.

Figure 2. Representative TEM images of HEp-2 cell sections after incubation for 1h with RSV in either serum-free medium (RSV) or medium with 50% HP (RSV+HP), 50% FBS (RSV+FBS). Compiled images of virions in close proximity to the cell-surface. Bar = 200nm.

Figure 3. Different corona pre-coatings affect RSV infectivity and moDC activation. (A) RSV virions produced under serum-free conditions were pre-coated with different coronae via pre-incubation with different biological fluids at the protein concentration of 0.3 mg/ml for 1h at 37 ºC prior to addition to HEp-2 cells in serum-free medium (diluted 10x) at an MOI of 1. RSV was incubated with the cells for 24 h before changing back to maintenance medium. The frequencies of eGFP expressing cells were quantified by flow cytometry 72 h post-infection. Gating strategy and uninfected control is shown in Supp Fig 4. Representative dot blot graphs are shown. **(B)** Flow cytometry quantification of the eGFP positive-cells after RSV pre-coating with different coronae from different biological fluids presented as fold-increase over RSV treatment in serum-free conditions. Mean of six replicates from two separate experiments. Non-parametric Kruskal-Wallis unpaired test followed by Dunn's post-test or Mann-Whitney test was used to compare the data. P-value: ** $P \leq 0.01$. Statistics were calculated using GraphPad Prism 7 software. (**C-F**) RSV virions produced under serum-free conditions were pre-incubated with different biological fluids, prior to the addition to primary moDCs in serum-free conditions at MOI of 20 for 4h. Cells were then washed and subsequently cultured in serum containing growth medium for 72h. CD86 expression and frequencies of RSV-GFP$^+$ cells were quantified by flow cytometry. (**C**) Representative histograms of CD86 expression in moDC are shown after different culture conditions; 1) RSV only 2) PolyI:C (25μg/ml) 3) non-infected supernatant 4) FBS only 5) RSV + FBS corona 6) BAL only 7) RSV + BAL corona. (**D**) The mean fluorescent intensity (MFI) of CD86 expression in moDCs infected with RSV pre-coated with different biological fluids for 1h prior to infection. Stimulation with TLR3 agonist PolyI:C was a positive control and negative controls included culture with BAL without any virus and sucrose used in the viral freezing medium. Significant differences were assessed by non-parametric Kruskal Wallis one-way ANOVA with Dunn's multiple comparison test and are indicated by ** P <.01 and **** P <.0001, respectively. NS indicates non-significant. Data are shown as MFI mean ± SEM for 6-8 individual donors from four separate experiments. (**E**) The frequency of RSV-GFP expressing moDCs treated with RSV pre-coated in different biological fluids for 1h prior to infection. Controls included culture with BAL without any virus and sucrose used in the viral freezing medium. Significant differences were assessed by non-parametric Kruskal Wallis one-way ANOVA with Dunn's multiple comparison test and are indicated by * P <.05 and **** P <.0001, respectively. Data are shown as frequencies of infected cells ± SEM for

6-8 individual donors from four separate experiments. (**F**) The frequencies of RSV-GFP expressing moDCs were quantified by flow cytometry 72 h post-infection comparing RSV pre-coated with different biological fluids. Representative dot blot graphs are shown.

Figure 4. RSV corona proteomic representation. (A) Venn-diagram showing the unique and overlapping protein populations from the RSV corona profiles in different biological fluids. The unique factors in HP and BAL are shown. (**B**) Gene list enrichment analysis of the total RSV corona profile in BAL and HP groups. The top five enriched terms are shown in each GO domain.

Figure 5. RSV accelerates the kinetics of amyloid formation. (**A**) 50 µl of 1mM NNFGAIL peptide incubated with 150 µl of 4 mM ThT solution and 100 µl of RSV (3×10^8 genome copy/ml) , non-infected supernatant or serum-free viral production medium (VP-SF medium). ThT fluorescence was measured at 440 nm excitation and 480 nm emission over 12 h at 37˚C. Means ±SEM of six replicates from two separate experiments are shown. (**B-C**) Negatively stained TEM images of RSV incubated with 1 mM NFGAIL for 100 mins. at 37˚C. (**B**) Fibrillar tangles are shown (**C**) RSV virion shown at the base of an amyloid fiber. White arrows indicate viral particle and black arrows indicate fibrillar structures. (**D**) NNFGAIL peptide incubated and monitored at similar conditions with 150 µl ThT solution and 100 µl of RSV in the presence or absence of 5% FBS, lipid vesicles (positively and negatively charged, dimeter= 200 nm, concentration = 1×10^{10} particles/ml) or VP-SF medium. (**E**) GNNQQNY peptide incubated with RSV, non-infected supernatant or VP-SF medium.

Figure 6. HSV-1 accelerates the kinetics of $A\beta_{42}$ fibrillation and interacts with amyloid fibrils. (A) 50 µl of 50 µM $A\beta_{42}$ peptide were incubated 150 µl of 4 mM ThT solution and 100 µl of HSV-1 (2×10^8 PFU/ml), non-infected supernatant or DMEM serum free growth medium. ThT fluorescence was measured at 440 nm excitation and 480 nm emission over 24 h at 37 ˚C. Means ±SEM of six replicates from two separate experiments are shown. (**B**) $A\beta_{42}$ incubated with HSV-1 in the presence or absence of 5% FBS (**C**) $A\beta_{42}$ incubated with either HSV-1 or lipid vesicles (positively or negatively charged, dimeter= 200 nm, concentration= 1×10^{10} particles/ml) incubated with $A\beta_{42}$ peptide (**D**) HSV-1 and DMEM serum free growth medium incubated with $A\beta_{42}$ or $A\beta_{40}$ peptides. (**E1-4**) Negatively stained TEM images of HSV-1 incubated with 50 µM $A\beta_{42}$ for 100 min. at 37 ˚C. White arrows indicate viral particles and black arrows indicate fibrillar structures. (**1**) Three protofilaments/fibrils stemming from one viral particle, bar = 200 nm. (**2**) Two protofilaments/fibrils stemming from a viral particle interacting with and aggregated structure, bar = 100 nm. (**3**) A viral particle interacting with protofilaments/fibrils which are connected to extensive fibrillar structures, bar =1 µm. (**4**) A rectangular close-up of viral interaction, bar = 500 nm. (**F-H**) Three-month-old transgenic 5XFAD mice were intracranially injected with HSV-1 or non-infected supernatant (NI). The mice were anesthetized 48 h after injection and brains were cryosectioned, fixed and stained using primary anti-body specific to isoforms Aβ 37-42 and then visualized by fluorescent Alexa 568 secondary antibody. The stained sections were imaged using 10x magnification, then (**F**) hippocampal and (**G**) cortical Aβ immunoreactivities were quantified from 6 stained sections at 400 um intervals per animal and are presented as positive area fraction percent. The accuracy of the analysis was confirmed by re-analyzing the images using ImageJ 1.50i software. N=8 in the HSV-1 group and N=7 in the NI group. Significant differences were assessed by Mann-Whitney test and are indicated by ***P <.001. Data are shown as frequencies of infected cells $\pm$ SEM for 6-8

individual donors from 2 separate experiments. (**H**) Representative images of the Aβ staining from HSV-1 vs. NI mice. Bar=500µm.

Supplementary Figure 1. Schematic representation of the setup for the proteomic studies of the viruses and controls. Viruses were produced in serum-free conditions and incubated in triplicates with different biological fluids. Negatively (-) and positively (+) charged lipid vesicles (liposomes) were incubated in triplicates under the same conditions. After incubation, samples were re-harvested be centrifugation, washed twice in PBS then analyzed with mass spectrometry. Crude biological fluids were also analyzed to determine the overall protein composition of the different fluids.

Supplementary Figure 2. Principal component analyses (PCA) of the corona proteomic profiles of HSV-1 and controls. Triplicate samples were incubated with 10% solutions of different biological fluids for 1h at 37 ˚C, then re-harvested, washed and finally analyzed by MS. (-)Lipo = negatively charged lipid vesicles, 200 nm, (+)Lipo = positively charged lipid vesicles, 200 nm. (**A**) PCA comparing proteomic profiles in human plasma (HP) (**B**) PCA comparing proteomic profiles in fetal bovine serum (FBS).

Supplementary Figure 3. Cryoimmuno-electron microscopy. Representative images of RSV incubated in serum-free conditions or with 50% v/v of different biological fluids then labelled with anti-RSV F protein antibody, anti-human IgG, or anti-surfactant protein A antibody. Black arrows indicate gold labelling. Bar = 200 nm.

Supplementary Figure 4. Methodology of FACS gating of (A-C) uninfected HEp-2 cells and (D-F) moDCs. Cells were first gated based on FSC/SSC (A and D), followed by gating on living cells (B and E) and lastly the $eGFP^+$ gate (C and F).

Supplementary Figure 5. Representative fluorescence microscopy pictures showing infectivity and syncytia formation in in HEp-2 cells using virus stocks that were derived in serum-free conditions or with different coronae resulting from pre-incubation with HP, FBS, BAL or MP. The upper row presents images the fluorescence channel and the lower row represents images of combined fluorescence and phase contrast channels.

Supplementary Figure 6. (**A**) Serum-free produced RSV was pre-coated with different coronae via pre-incubation with biological fluids at the stated protein concentration for 1h at 37º C prior to infection of HEp-2 cells in serum-free medium (diluted 10x) at an MOI of 1. RSV was incubated with the cells for 24h before changing back to maintenance medium. The frequencies of eGFP expressing cells were quantified by flow cytometry 72h post-infection. Data represents mean of six replicates from two separate experiments. Significant differences were assessed by non-parametric Kruskal Wallis one-way ANOVA with Dunn's multiple comparison test and are indicated by $*P$ <.05, $**P$ <.01 and $***P$ <.001, respectively. (**B**) Neutralization curves with different concentrations of palivizumab (monoclonal antibody targeting RSV F-protein) of RSV with or without FBS and MP protein coronae. Data represents mean ±SEM of six replicates from two separate experiments

Supplementary Figure 7. Different biological fluids were diluted to a protein concentration of 0.3 mg/ml, and then ELISA was used to quantify RSV specific IgG antibodies.

Supplementary Figure 8. (**A**) The unique factors in FBS and MP from Fig. 4 are listed. (B) Gene list enrichment analysis of the total RSV corona profile in FBS and MPP groups. The top five enriched terms are shown in each GO domain.

Supplementary Figure 9. (**A-B**) Curves representing the background interaction of ThT with the growth media, RSV or HSV-1 in absence of peptides.

Figures

Figure 1.

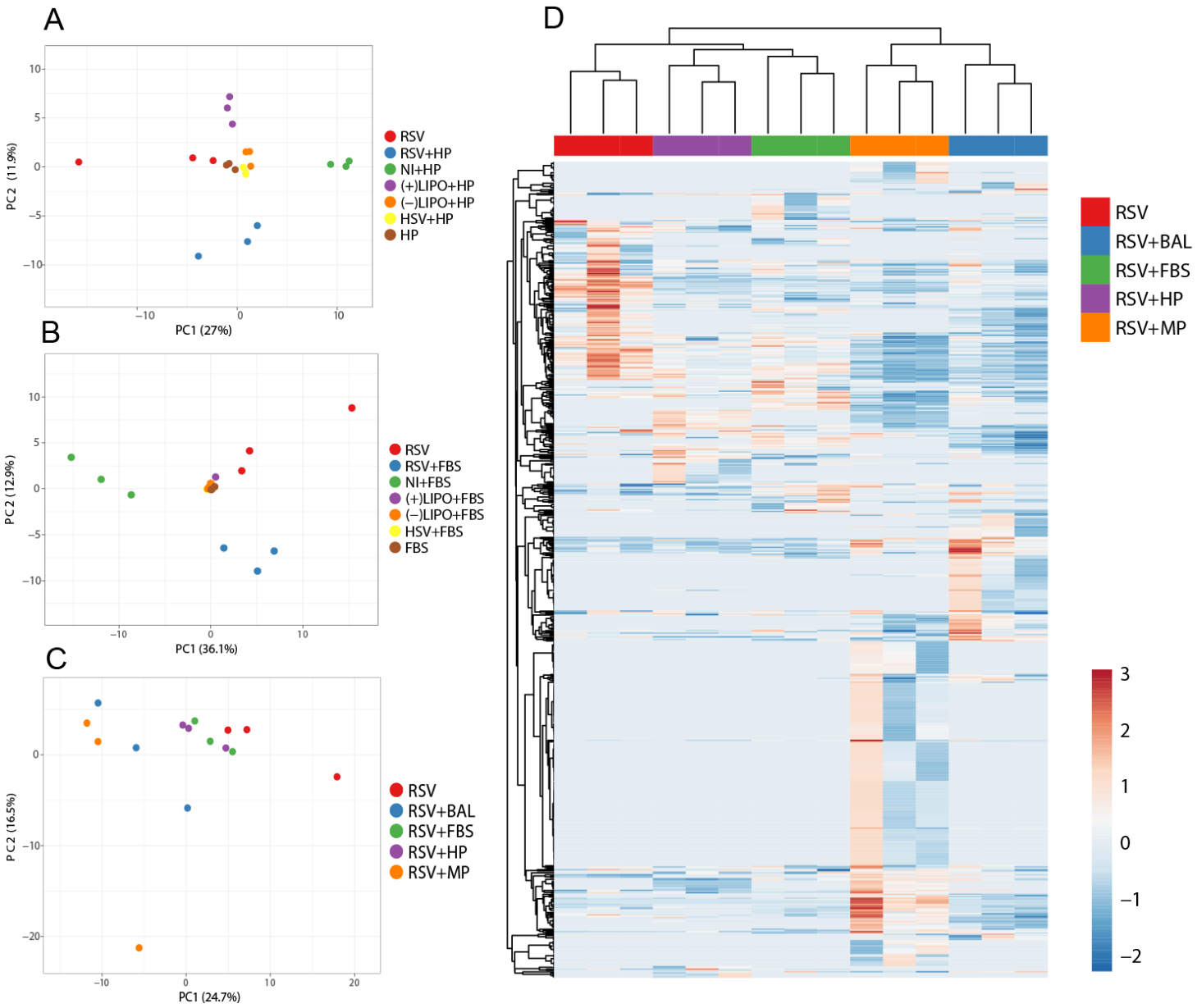

Figure 2

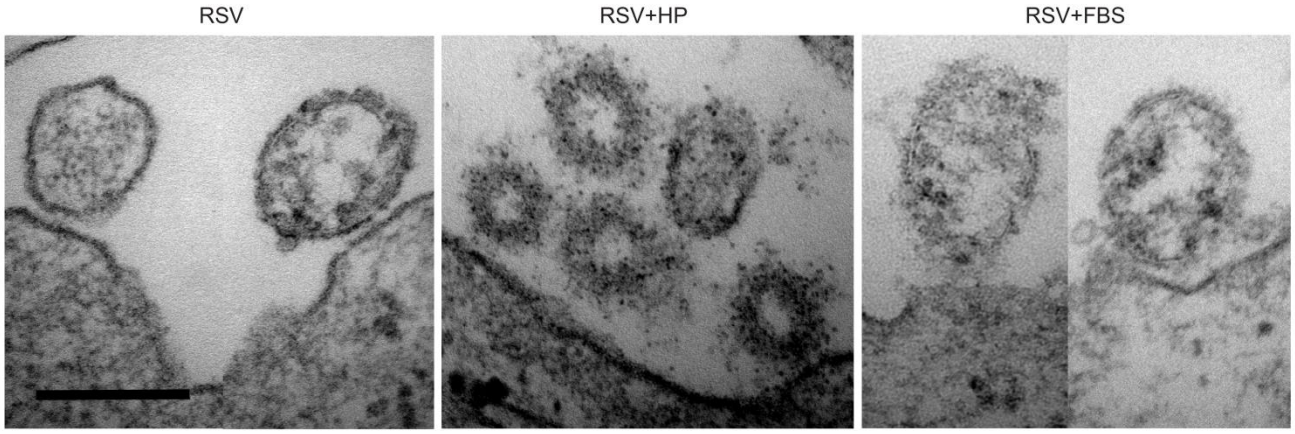

Figure 3

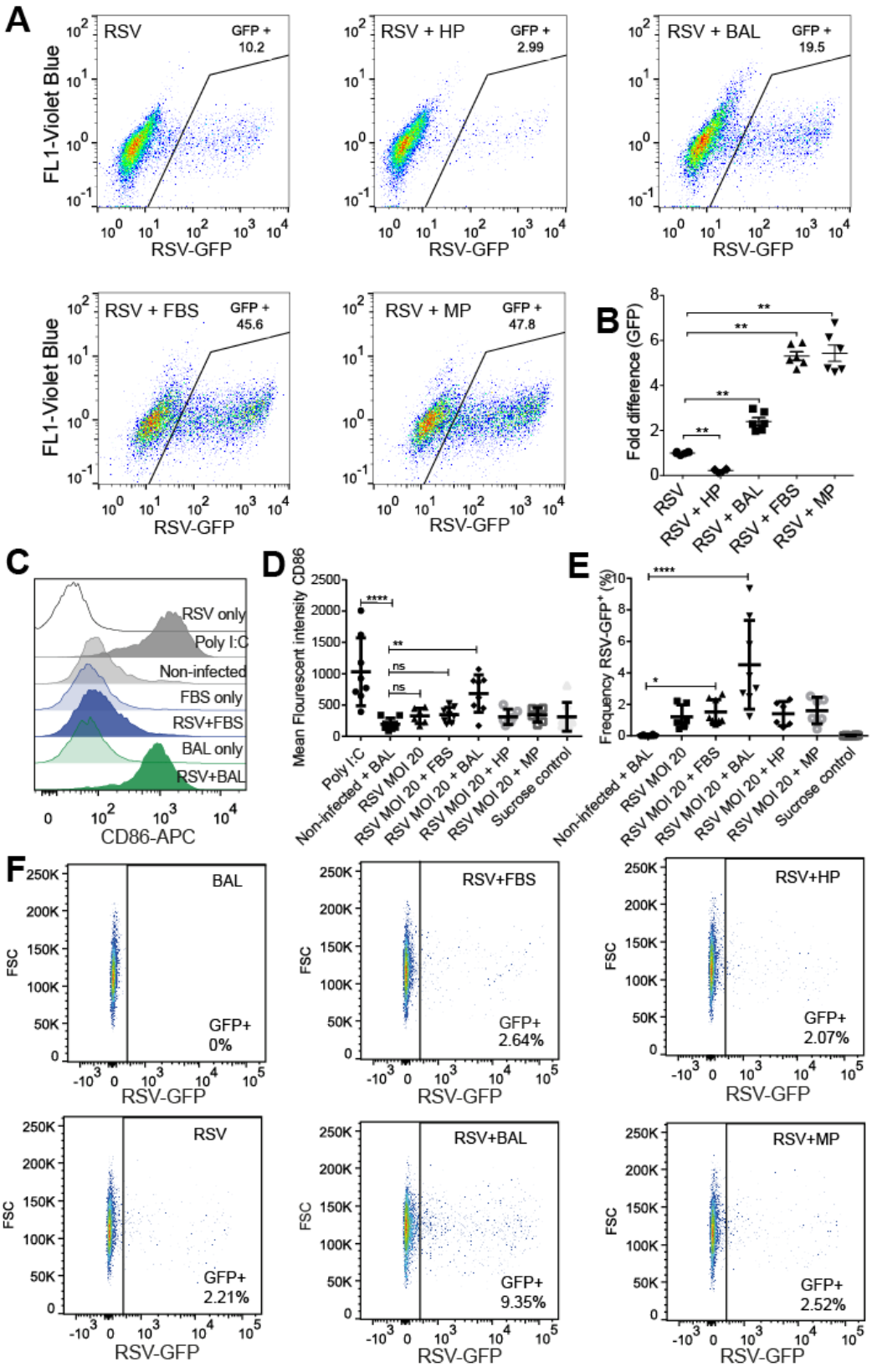

Figure 4

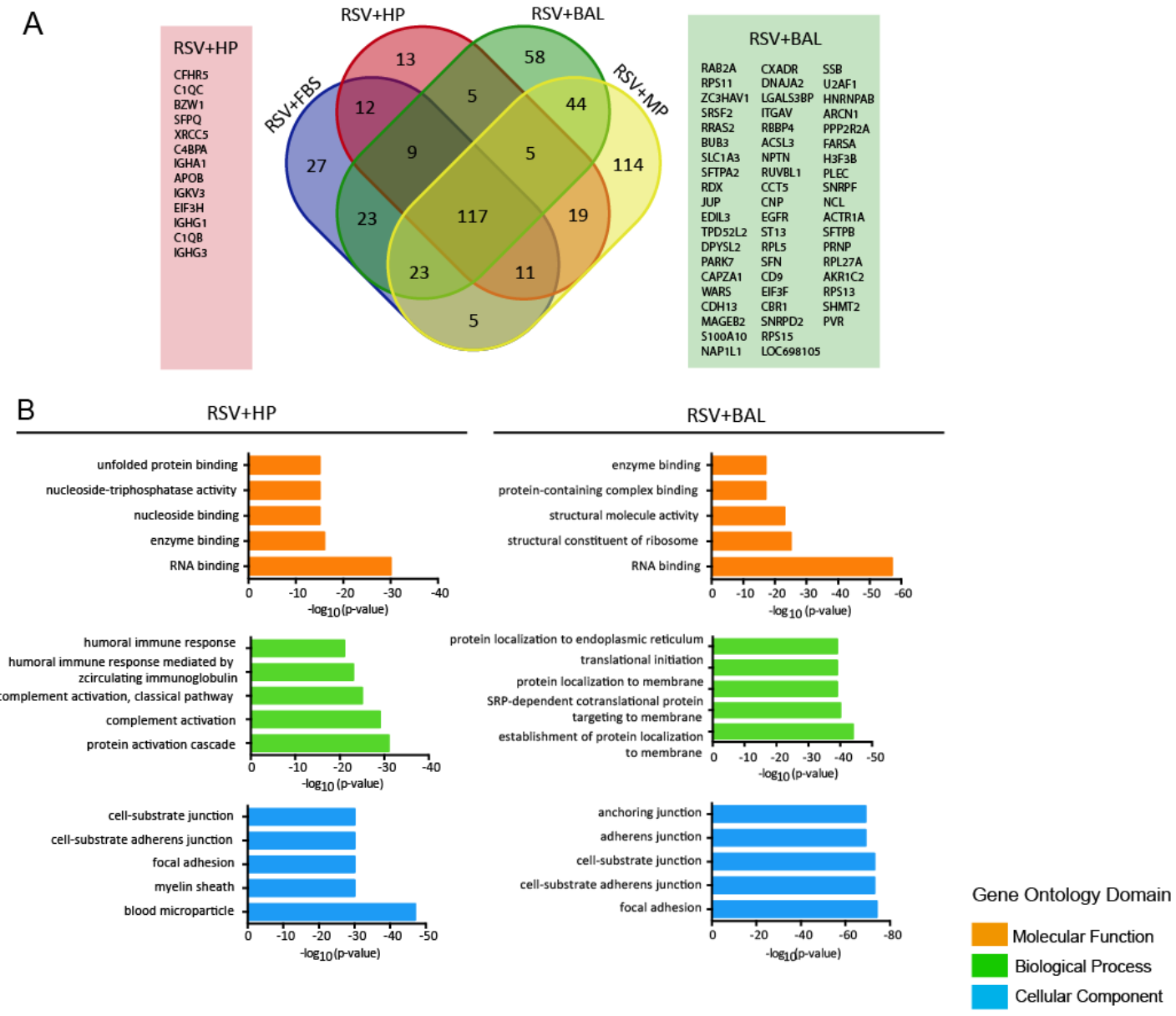

Figure 5

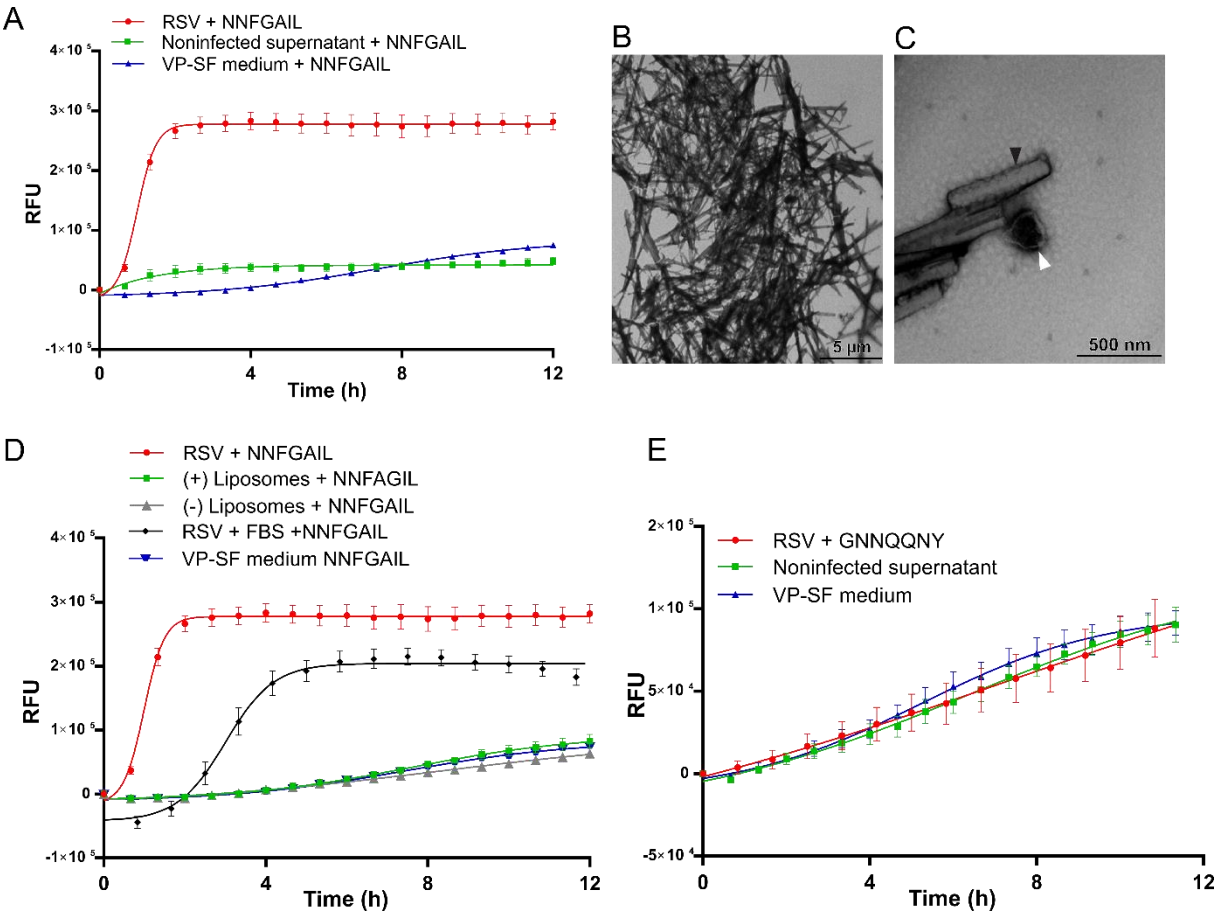

Figure 6

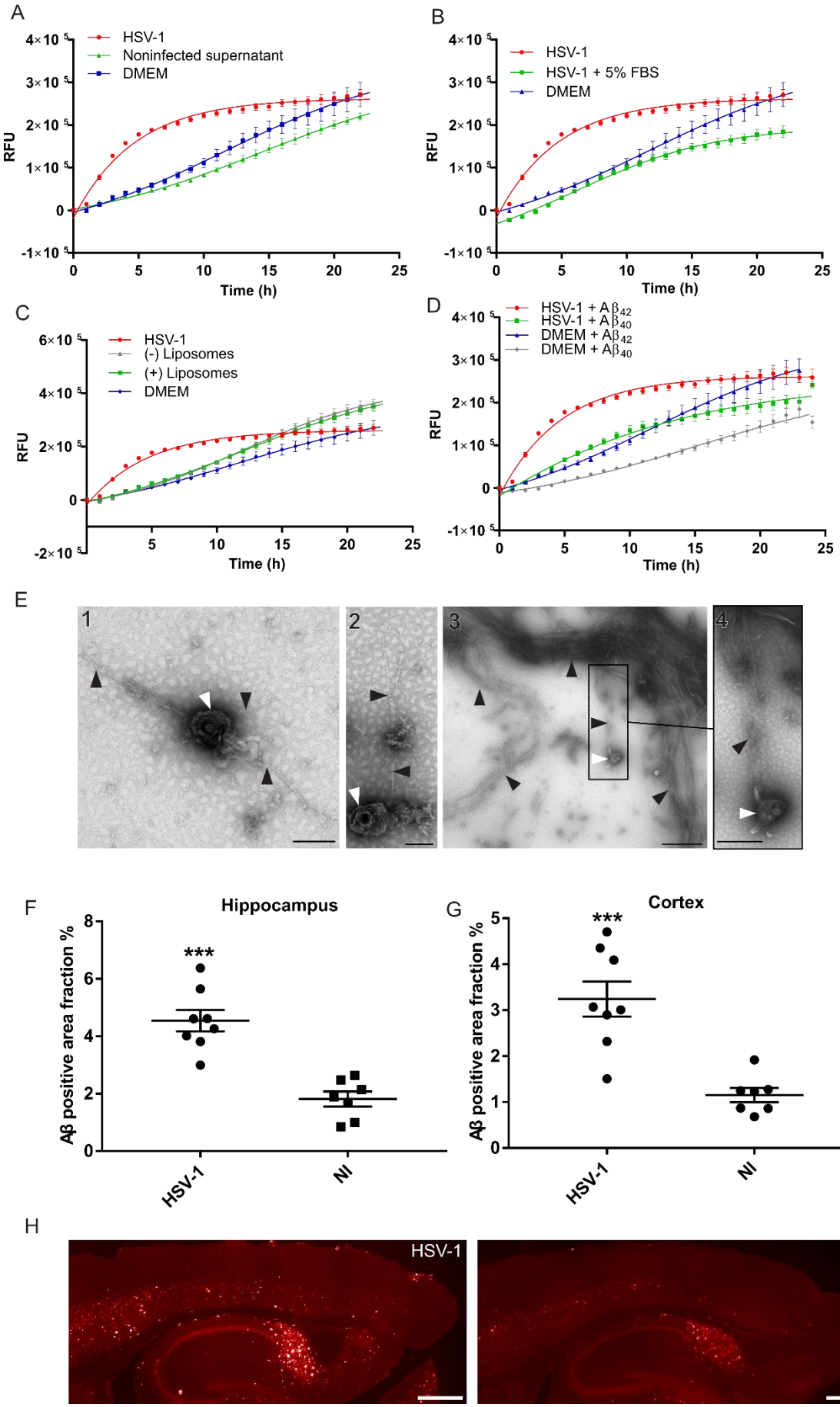

Supp. Fig. 1

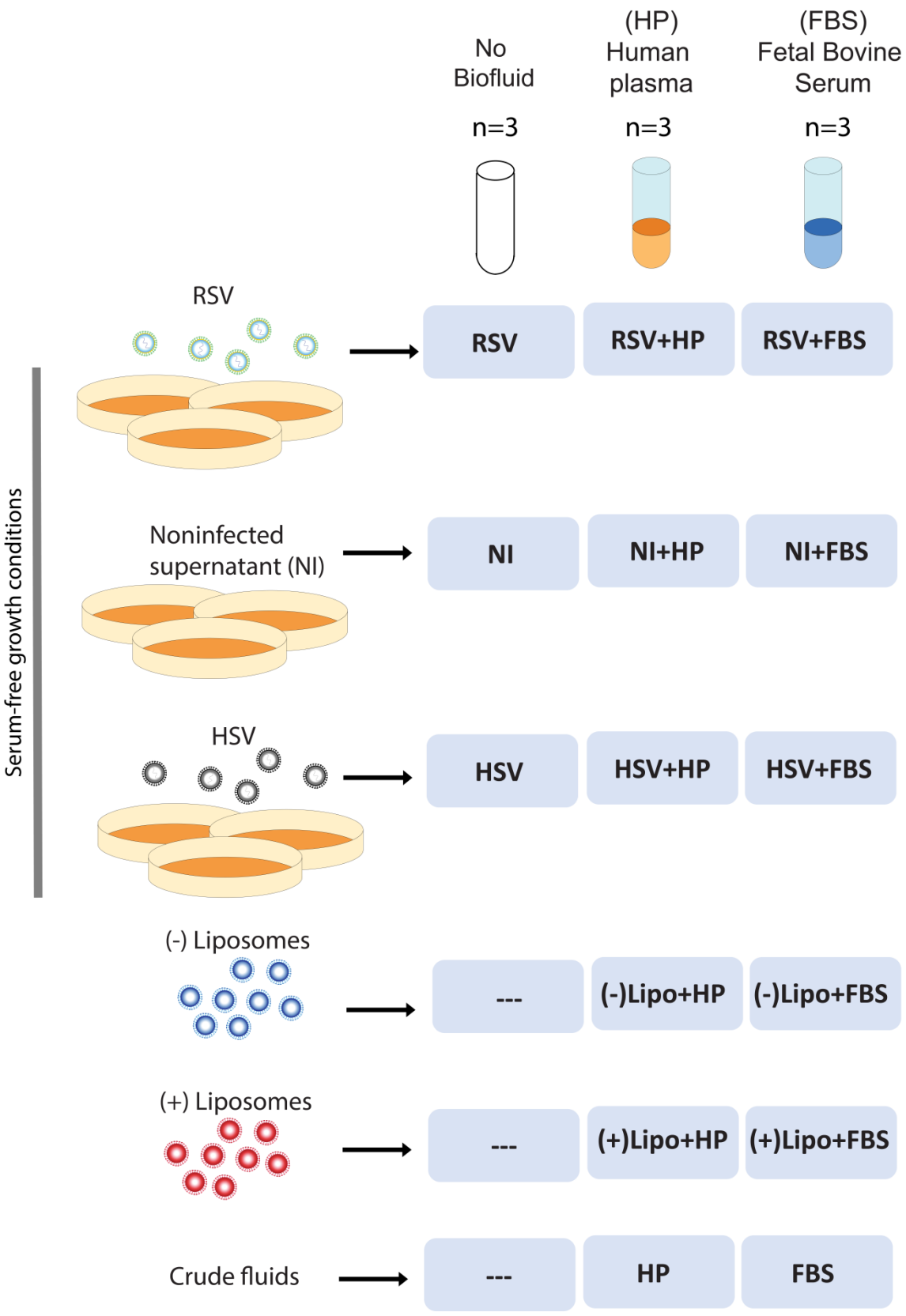

Supp. Fig. 2

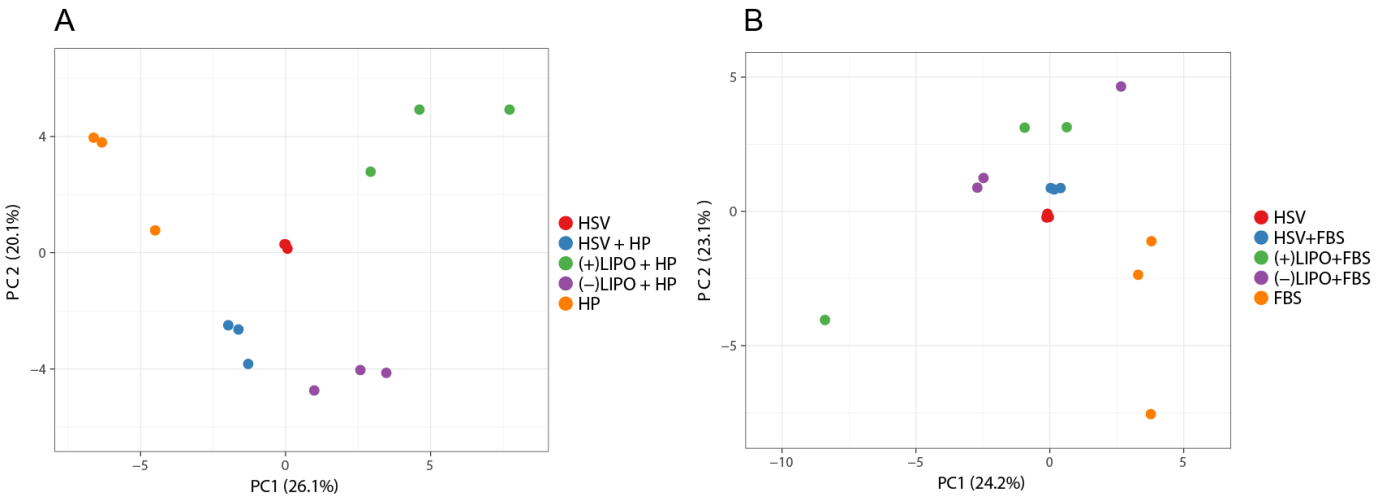

Supp. Fig. 3

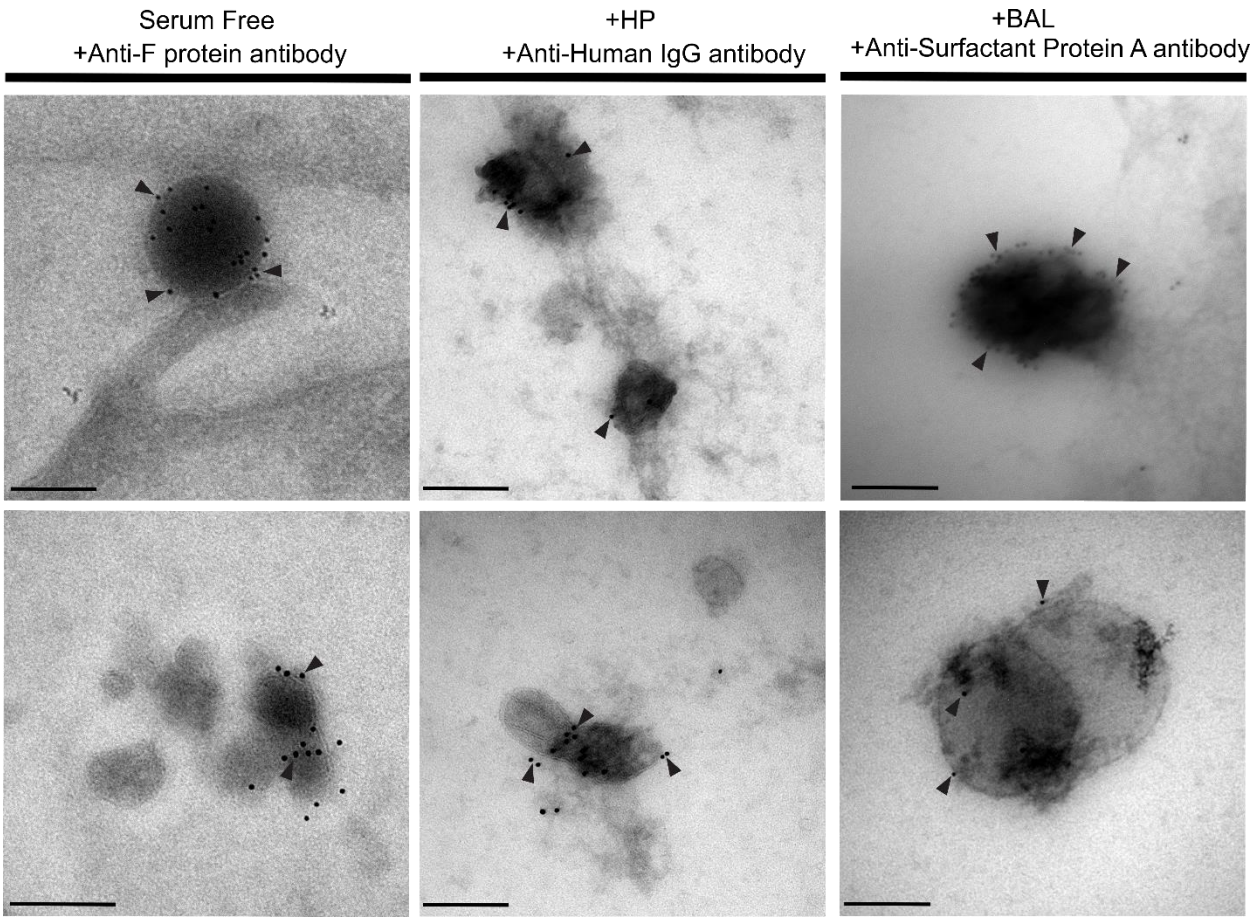

Supp. Fig. 4

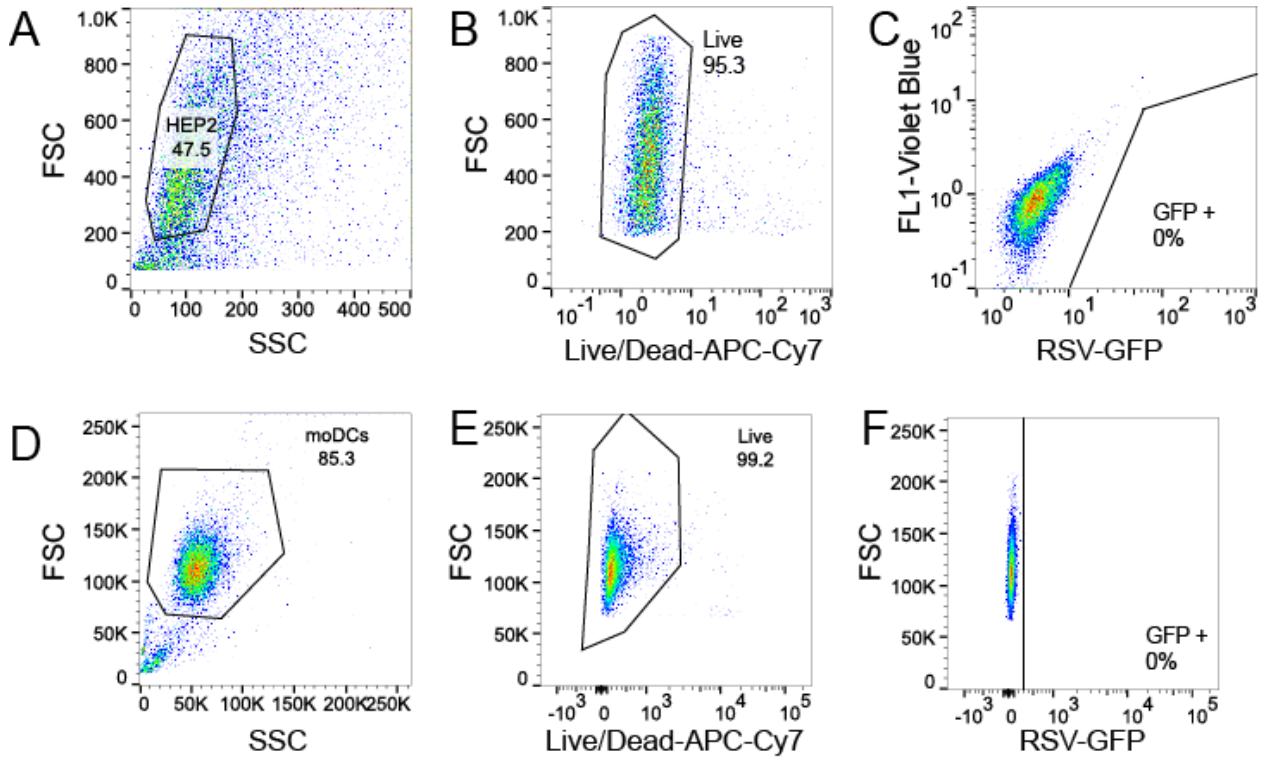

Supp. Fig. 5

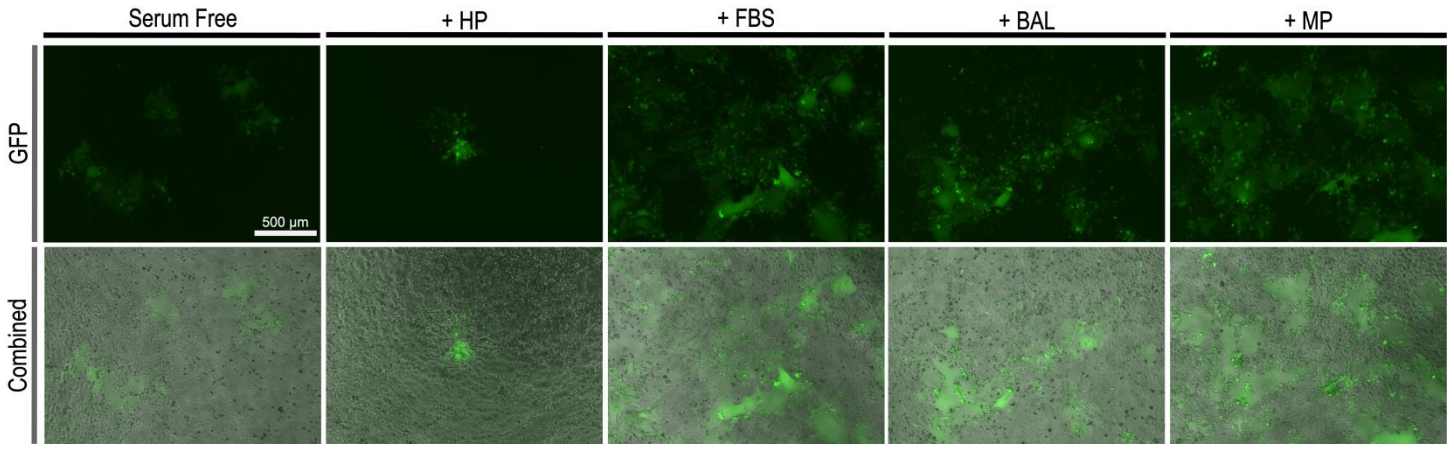

Supp. Fig. 6

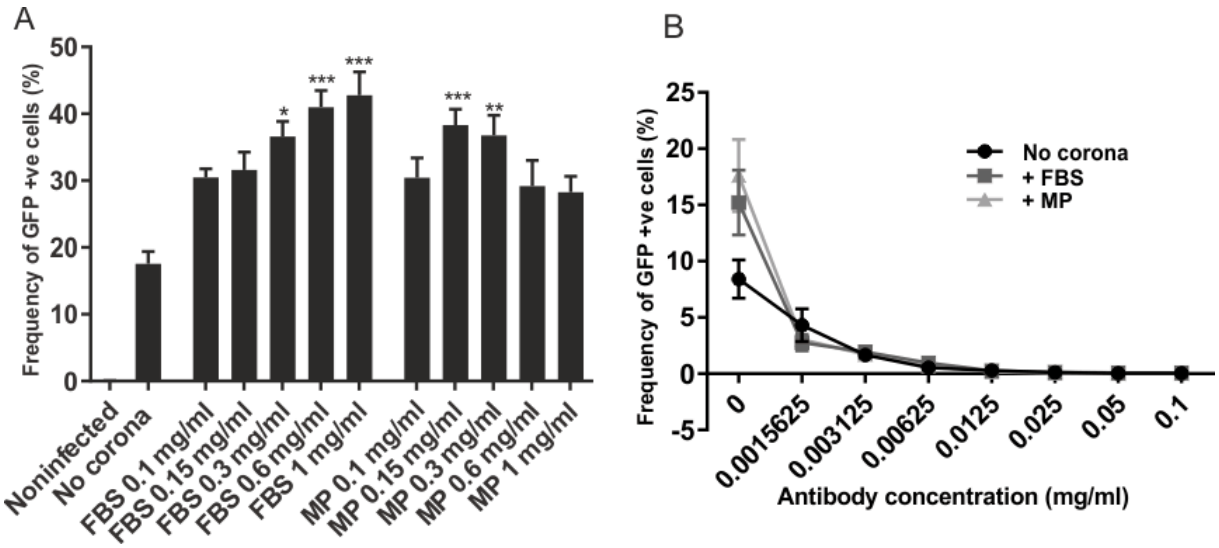

Supp. Fig. 7

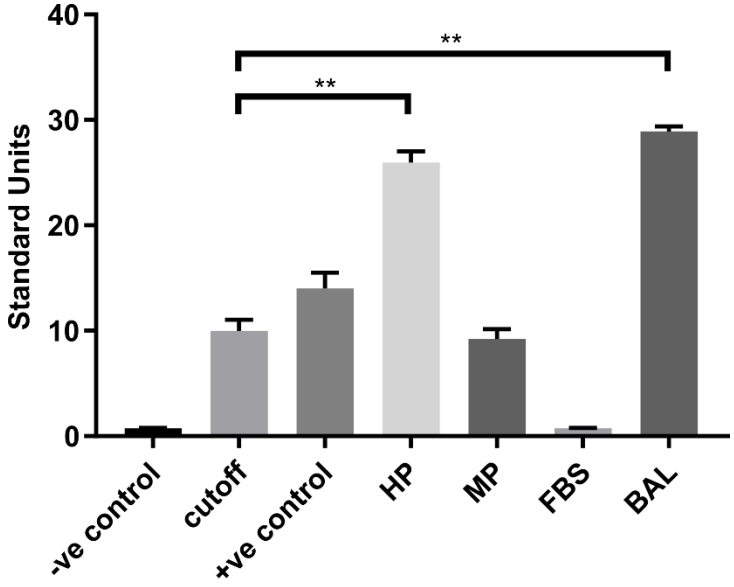

Supp. Fig. 8

A

RSV+FBS

FERMT2
RTN4
ETFA
PHB2
DNAJB1
RPN1
SERPINE2
NME2
TNPO1
PSMC3
TSNAX
LOC510860
HBA
PRDX5
MGC137099
XRCC6
GPI
PDHB
LOC617696
HNRNPU
GDI2
PSMC6
CDC37
CKAP4
PARP1
CCT7
HBA1

RSV+MP

LOC721200	BST2	SRGN	EGK_14881
EGK_17555	ESAM	VDAC3	APP
SLC4A1	LOC723514	ACTN1	g6g
DECR1	CORO1C	KIF5B	COMT
ILK	SDPR	ARL6IP5	EGK_05213
COX5A	LOC714514	IDH2	LOC106992286
EGK_19779	EGK_08806	MDH2	FN1
HSD17B10	Mamu	CORO1A	PPP2CA
ESYT1	EGK_02861	PARVB	HBA2
CCL5	ETFB	ASS1	PRDX2
GP1BA	IGKC	UQCRC1	YWHAB
GC	HBD	PPIF	RAB8A
YWHAH	EGK_04537	SPTB	
RAB27B	EGK_09508	LOC720309	
VASP	FHOD1	THBS1	
EGK_05927	SNAP23	BKB3	
GSN	PCBP2	LTBP1	
DLST	ITGB3	PPBP	
C5	VWF	CS	
MYL9	EGK_03005	EGK_12095	
SQRDL	MYL12A	EGK_08849	
ZYX	TPM1	ITGA1	
MYL12B	MBOAT7	SPTA1	
F13A1	PF4	ANK1	
SLC2A14	RRAS	FERMT3	
MT1	EGK_03266	ALDOA	
SELP	EGK_08779	ARPC1B	
PLEK	MMRN1	EGK_08894	
HS1	EGK_16635	RHOA	
ITGA2B	PTGS1	EGK_10733	
GPD2	EGK_08321	EGK_15803	
PSAP	SUCLG2	ARPC4	
TPM2	GNAQ	TUBB1	
CAM1	EGK_08059	JCHAIN	

B

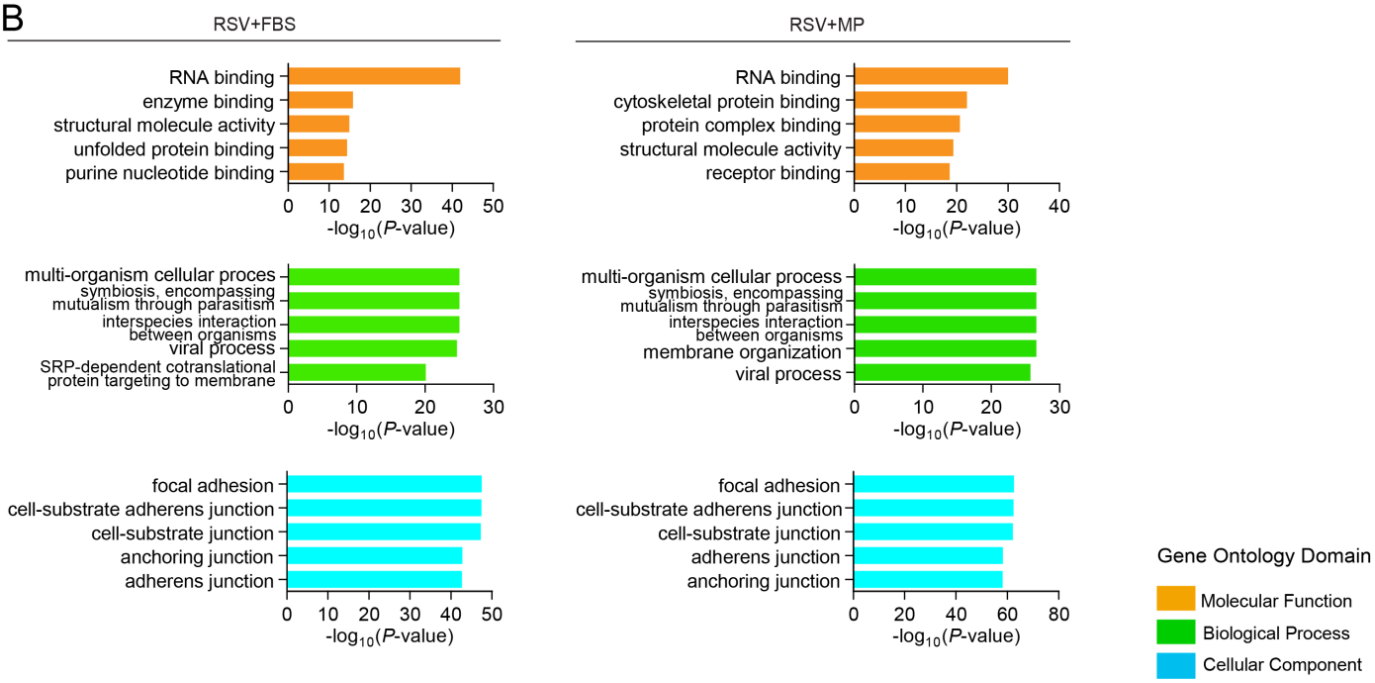

Supp. Fig. 9

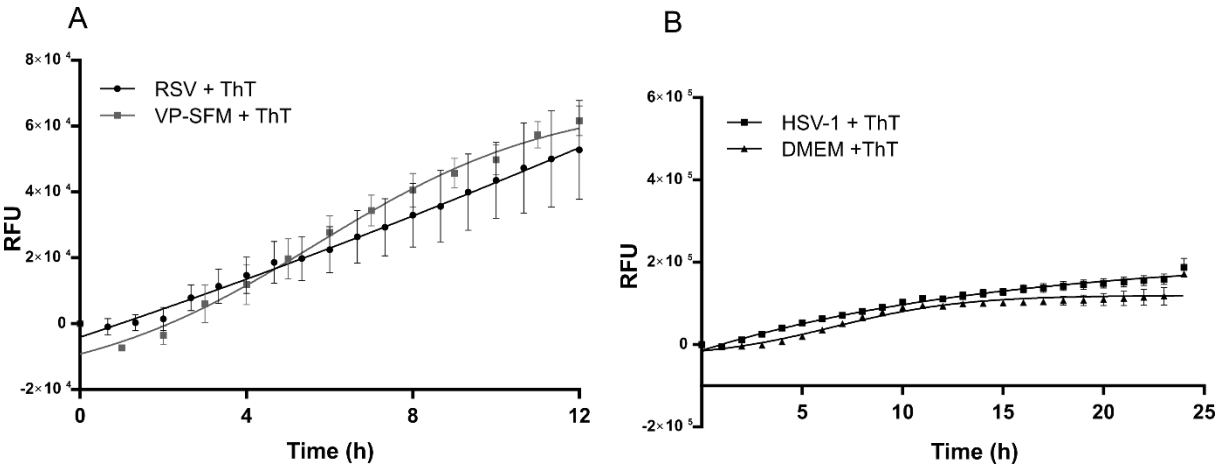

Table 1. Top 10 proteins in the RSV corona vs. the crude biological fluids.

Top10 Corona	Top 10 biofluid
RSV+HP	**HP**
Beta-actin-like protein 2 [ACTBL_HUMAN]	Serum albumin [ALBU_HUMAN]
Actin, cytoplasmic 1[ACTB_BOVIN]	Ig alpha-1 chain C region [IGHA1_HUMAN]
Actin, alpha skeletal muscle [ACTS_BOVIN]	Serotransferrin [TRFE_HUMAN]
Complement C4-B [CO4B_HUMAN]	Ig alpha-2 chain C region [IGHA2_HUMAN]
Complement C4-A [CO4A_HUMAN]	Protein IGKV3-11 [A0A087WZW8_HUMAN]
Complement C3 [CO3_HUMAN]	Ig lambda-3 chain C regions (Fragment) [A0A075B6L0_HUMAN]
Complement component 3 [A0A0F6QNP7_BOVIN]	Ig lambda-1 chain C regions (Fragment) [A0A075B6K8_HUMAN]
Tubulin alpha-1C chain [TBA1C_HUMAN]	Haptoglobin OS [HPT_HUMAN]
Nucleoprotein [NCAP_HRSVA]	Isoform 2 of Fibrinogen alpha chain [FIBA_HUMAN]
Glyceraldehyde-3-phosphate dehydrogenase [G3P_HUMAN]	Hemopexin OS [HEMO_HUMAN]
RSV+FBS	**FBS**
Actin, cytoplasmic 1 [ACTB_BOVIN]	Serum albumin [A0A140T897_BOVIN]
Beta-actin-like protein 2 [ACTBL_HUMAN]	ALB protein [B0JYQ0_BOVIN]
Actin, alpha skeletal muscle [ACTS_BOVIN]	Alpha-2-HS-glycoprotein [FETUA_BOVIN]
Tubulin alpha-1C chain [TBA1C_HUMAN]	Serotransferrin [G3X6N3_BOVIN]
Glyceraldehyde-3-phosphate dehydrogenase [G3P_HUMAN]	Serotransferrin [TRFE_BOVIN]
Nucleoprotein [NCAP_HRSVA]	Fetuin-B [FETUB_BOVIN]
Phosphoprotein [PHOSP_HRSVA]	Protein AMBP [F1MMK9_BOVIN]
Tubulin alpha-4A chain [TBA4A_BOVIN]	Vitamin D-binding protein [VTDB_BOVIN]
Heat shock 70 kDa protein 1A [HS71A_HUMAN]	Vitamin D-binding protein [F1N5M2_BOVIN]
Glyceraldehyde-3-phosphate dehydrogenase [I2CWU4_MACMU]	Alpha-1B-glycoprotein [A1BG_BOVIN]
RSV+MP	**MP**
Actin, cytoplasmic 1 [ACTB_BOVIN]	Serum albumin (Fragment) [ALBU_MACMU]
Actin, alpha skeletal muscle [ACTS_BOVIN]	Uncharacterized protein [G7MT40_MACMU]
Beta-actin-like protein 2 [ACTBL_HUMAN]	Uncharacterized protein [G7MJR4_MACMU]
Phosphoprotein [PHOSP_HRSVA]	Transferrin OS [F7DHR8_MACMU]
Tetraspanin (Fragment) [G7N5L6_MACMU]	Fibrinogen alpha chain [F6UZ60_MACMU]
Serum albumin (Fragment) [ALBU_MACMU]	Putative uncharacterized protein [F6WR34_MACMU]
Uncharacterized protein [G7MT40_MACMU]	Uncharacterized protein [F6UZ87_MACMU]
Matrix protein [MATRX_HRSVA]	Haptoglobin isoform 2 preproprotein [H9Z8D4_MACMU]
Glyceraldehyde-3-phosphate dehydrogenase [G3P_HUMAN]	Uncharacterized protein [A0A1D5QT02_MACMU]
Isoform 2 of 4F2 cell-surface antigen heavy chain [4F2_HUMAN]	Hemoglobin subunit beta [HBB_MACMU]
RSV+BAL	**BAL**
Actin, alpha skeletal muscle [ACTS_BOVIN]	Serum albumin [ALBU_HUMAN]
Actin, cytoplasmic 1 [ACTB_BOVIN]	Serotransferrin [TRFE_HUMAN]
Beta-actin-like protein [ACTBL_HUMAN]	Ig alpha-1 chain C region [IGHA1_HUMAN]
Phosphoprotein [PHOSP_HRSVA]	Uteroglobin [UTER_HUMAN]
Glyceraldehyde-3-phosphate dehydrogenase [G3P_HUMAN]	Lysozyme C [LYSC_HUMAN]
Matrix protein [MATRX_HRSVA]	Ig alpha-2 chain C [IGHA2_HUMAN]
Nucleoprotein OS [NCAP_HRSVA]	Protein IGKV3-11 [A0A087WZW8_HUMAN]
Isoform 2 of Heat shock protein 75 kDa, mitochondrial [TRAP1_HUMAN]	Antileukoproteinase [SLPI_HUMAN]
Pulmonary surfactant-associated protein A2 [SFPA2_HUMAN]	Ig lambda-3 chain C regions (Fragment) [A0A075B6L0_HUMAN]
Isoform 2 of 4F2 cell-surface antigen heavy chain [4F2_HUMAN]	Ig lambda-1 chain C regions (Fragment) [A0A075B6K8_HUMAN]

Supp. Table 1: Top 10 proteins in the HSV-1 corona vs. the crude biological fluids.

Top10 Corona	Top 10 biofluid
HSV+HP	**HP**
Ig gamma-1 chain C region [A0A087X079_HUMAN]	Serum albumin [ALBU_HUMAN]
Complement C3 [CO3_HUMAN]	Ig alpha-1 chain C region [IGHA1_HUMAN]
Complement component 3 [A0A0F6QNP7_BOVIN]	Serotransferrin [TRFE_HUMAN]
Ig gamma-3 chain C region (Fragment) [A0A075B6N8_HUMAN]	Ig alpha-2 chain C region [IGHA2_HUMAN]
Envelope glycoprotein D [GD_HHV1F]	Protein IGKV3-11 [A0A087WZW8_HUMAN]
Protein IGKV3-11 [A0A087WZW8_HUMAN]	Ig lambda-3 chain C regions (Fragment) [A0A075B6L0_HUMAN]
Complement C4-B [CO4B_HUMAN]	Ig lambda-1 chain C regions (Fragment) [A0A075B6K8_HUMAN]
Complement C4-A [CO4A_HUMAN]	Haptoglobin OS [HPT_HUMAN]
Tegument protein UL47 [TEG5_HHV1F]	Isoform 2 of Fibrinogen alpha chain [FIBA_HUMAN]
Envelope glycoprotein E [GE_HHV1F]	Hemopexin OS [HEMO_HUMAN]
HSV+FBS	**FBS**
Chromatin assembly factor 1 subunit B [A5D9H4_BOVIN]	Serum albumin [A0A140T897_BOVIN]
PRPF8 protein [A7Z025_BOVIN]	ALB protein [B0JYQ0_BOVIN]
Angiotensinogen [ANGT_HUMAN]	Alpha-2-HS-glycoprotein [FETUA_BOVIN]
Thyroglobulin [F1MPH3_BOVIN]	Serotransferrin [G3X6N3_BOVIN]
Serglycin [SRGN_HUMAN]	Serotransferrin [TRFE_BOVIN]
Histone H2B type 1-N [H2B1N_BOVIN]	Fetuin-B [FETUB_BOVIN]
Keratin, type II cytoskeletal [K2C6A_HUMAN]	Protein AMBP [F1MMK9_BOVIN]
Period circadian protein homolog 3 [A0A087WV69_HUMAN]	Vitamin D-binding protein [VTDB_BOVIN]
Uncharacterized protein [H9H2P7_MACMU]	Vitamin D-binding protein [F1N5M2_BOVIN]
Uncharacterized protein [F6WIY2_MACMU]	Alpha-1B-glycoprotein [A1BG_BOVIN]